Nonlinear numerical simulation of the soil seismic response to the 2012 Mw 5.9 Emilia earthquake considering the variability of the water table position

Maria Paola Santisi d'Avila, Luca Lenti, Salvatore Martino

Nonlinear numerical simulation of the soil seismic response to the 2012 Mw 5.9 Emilia earthquake considering the variability of the water table position

Maria Paola Santisi d'Avila[1], Luca Lenti[2], Salvatore Martino[3] and Roberto Walter Romeo[4+]

[1] Université Côte d'Azur, LJAD, Nice, France

[2] Université Paris Est, IFSTTAR, Paris, France

[3] Università Roma La Sapienza, CERI, Roma, Italy

[4] Libera Università di Urbino Carlo Bo, Urbino, Italy

[+] deceased

Corresponding author:

Maria Paola Santisi d'Avila

Université Côte d'Azur - LJAD

28, Avenue Valrose - 06108 Nice - France

Email: msantisi@unice.fr

ABSTRACT

This research is focused on the case study of San Carlo village (Emilia Romagna, Italy), struck by the 20 May 2012 Mw 5.9 Emilia earthquake that caused severe damage due to widely observed soil liquefaction. More in particular, it is investigated the influence on nonlinearity effects of the variability of the water table depth, due to seasonal fluctuation.

The one-directional propagation of a three-component seismic wave (1D-3C approach), in a multilayered soil profile, is simulated using a finite element model and an elasto-plastic constitutive behavior with hardening for the soil (Iwan's model). The nonlinearity is described by the normalized shear modulus decay curve obtained by resonant column tests. The shear modulus is corrected during the process (Iai's model) to consider the cyclic mobility and dilatancy of sands, depending on the actual average effective stress and the friction and dilatancy angles obtained from cyclic consolidated undrained triaxial tests.

Profiles with depth of maximum excess pore water pressure, horizontal motion and shear strain and stress are obtained in the case of effective stress analysis, for an average position of the water table depth and for a variation of ±1 m, and then compared with a total stress analysis. The variability with the water table depth of soil profile response to seismic loading is observed also in terms of hysteresis loops, time histories of the ground motion and excess pore water pressure in the liquefiable soil layers prone to cyclic mobility process.

Keywords: saturated soil, liquefaction front, wave propagation, Finite Element Method, Emilia earthquake.

INTRODUCTION

During the 20 May 2012 Mw 5.9 Emilia earthquake (Italy), liquefaction phenomena have been observed (Chini et al., 2015; Emergeo Working Group, 2013). Several studies (Facciorusso et al. 2014, 2015; Vannucchi et al., 2012; Papathanassiou et al., 2015) demonstrate that predisposing conditions to soil liquefaction could be recognized in several sites (including the villages of San Carlo, Mirabello and Sant'Agostino) where such an effect was induced by the 2012 Emilia earthquake. Focusing on this case study, the impact of water table depth on the earthquake-induced effects in soil columns is here analyzed.

Effects due to co-seismic water level changes, inducing soil liquefaction, are observed and discussed by Wang et al. (2003) while Wayne and Dohering (2006) observe liquefaction induced by measured water level changes after detonation in underground of chemical and nuclear explosives. Some authors (Nishikawi et al., 2009; Yasuda and Ishikawa, 2015) discuss the possible role of water table lowering for the soil improvement against co-seismic liquefaction occurrence and building damage. Moreover, a co-relation of shallow groundwater levels with the liquefaction occurrence is proposed by Hartantyo et al., 2014 for the May 2006 Earthquake at Yogyakarta (Indonesia). Some analytical evaluations are performed to consider the effect of water level on analytical indexes for liquefaction susceptibly as well as on induced post-seismic settlements (Chung and Rogers, 2013).

In this research, a numerical modeling is developed to simulate the seismic response of the soil columns through effective stress analysis (ESA). A vertical wave propagation model is adopted under the assumption of horizontally extended soil. The one-directional (1D) wave propagation modeling, compared with a three-dimensional (3D) one, reduces modeling difficulties and computation time, and guarantees a reliable geotechnical model, easy to characterize with

limited geotechnical investigations. The finite element model adopted to simulate the propagation of three-component (3C) seismic waves, in a multilayered subsoil, is implemented in SWAP_3C code (Santisi et al., 2012) that has been verified and validated during the PRENOLIN benchmark (Regnier et al., 2018) in the case of total stress analysis (TSA) and nonlinear soil behavior.

The Iwan's elasto-plastic model (Iwan, 1967; Joyner, 1975; Joyner and Chen, 1975) is adopted to represent the 3D nonlinear behavior of soil. Its main feature is the faithful reproduction of nonlinear and hysteretic behavior of soils under cyclic loadings, with a reduced number of parameters characterizing the soil properties. The model is calibrated using the elastic moduli in shear and compression and the shear modulus decay curve is employed to deduce the size of the yield surface.

The correction of the shear modulus proposed by Iai et al. (1990a,b) is employed for saturated cohesionless soil layers to consider the cyclic mobility and dilatancy of sands. Liquefaction front parameters are calibrated by a trial-and-error procedure to best reproduce the curves obtained by cyclic consolidated undrained triaxial (CTX) tests, that represent the deviatoric strain amplitude and normalized excess pore water pressure with respect to the number of cyclic loading. Bonilla *et al.* (2005) propose the Iwan's hysteretic model combined with the Iai's liquefaction front model. The model is applied to a one-directional one-component seismic wave propagation, in a finite difference formulation. Oral *et al*. (2017) use the extension of Iai's shear modulus correction to a multiaxial stress state, induced by a 3C excitation. The model is adopted in a spectral element formulation, for a three-component seismic loading propagating in a 1D soil profile. Santisi d'Avila et al. (2018) discuss the 3D Iwan-Iai model and compare the behavior of dense and loose sands under one- and three-component loading. They also validate the one-

88 directional three-component (1D-3C) wave propagation model in liquefiable soils, for the case
89 of KSRH10 Japanese soil profile, whose geotechnical data are provided by the reports of
90 PRENOLIN benchmark.
91 Stratigraphy and geotechnical parameters of three soil profiles in San Carlo village (Emilia
92 Romagna, Italy) are accurately identified based on available data and specifically performed
93 borehole investigations. The simulation of their response to the 20 May 2012 Mw 5.9 Emilia
94 earthquake is initially performed by considering an average depth of the water table. In the
95 following, the influence of the water table depth variability on the seismic response of the
96 investigated soil profiles is accounted for and the obtained results are discussed, in terms of
97 ground motion at the surface and profiles with depth of maximum stress, strain and soil motion.
98 The case study is of particular interest for the Italian National Civil Protection since it pointed
99 out emergency conditions induced by liquefaction effects. Moreover, due to the similarity of
100 geological setting of the area felt by the 2012 Emilia earthquake with large zones of the Pianura
101 Padana plain (northern Italy) this case study exemplifies conditions that could be somewhere
102 else expected.
103 Due to the co-seismic nature of the nonlinear effects related to soil liquefaction, this study
104 contributes to depict quantitative provisional scenarios for risk mitigation by identifying
105 geological setting prone to liquefaction and supporting the outline of unstable zones in the
106 framework of Seismic Microzonation studies (DPC-CRP, 2008).
107

108 **CASE STUDY**

109 On May 2012 a seismic sequence hit the river Po valley plain in Northern Italy, with two
110 mainshocks of magnitude close to 6 (Scognamiglio et al., 2012) which triggered several ground

111 effects mainly represented by liquefaction (Fig. 1a,b) in all its variegated phenomena (i.e. sand
112 boils crack fissures, lateral spreading, settlements). Such effects significantly contributed to
113 increase the structural damages due to the seismic shaking (Fig. 1c,d).
114 The investigated site was shaken by earthquakes of similar magnitude which produced similar
115 ground effects in the past (Martino et al., 2014), as reported in the Italian catalogue of
116 earthquake-induced ground effects (CEDIT, see Data and Resources). The seismic sequence,
117 well described in Scognamiglio et al. (2012), consisted of two mainshocks, the first of which
118 (M_w 5.9 on May 20th, 2012) was responsible for the liquefaction effects at the investigated site
119 (16 km far from the epicentre). The inferred peak ground acceleration according to the
120 automated shakemaps (INGV, see Data and Resources) is about $0.32\,g$.
121 After the seismic sequence, many investigations are carried out, both on site and in laboratory,
122 in order to explore the soil susceptibility to undergo failure. Some studies are already published
123 attempting to explain the triggering mechanisms of the observed phenomena (Vannucchi et al.,
124 2012; Emergeo Working Group, 2013; Facciorusso et al., 2014; Papathanassiou et al., 2015;
125 Chini et al., 2015; Caputo et al., 2015).
126 The geomorphological features of the studied area are sculptured into the alluvial plain formed
127 by the digressions of a riverbed (Reno river), whose course was continuously changed by man in
128 the past centuries with the aim to control its disastrous floods (Bondesan, 1990; 2001). The
129 original river course was definitely abandoned in the 18th century, so the area where the San
130 Carlo village lies is characterized by the old riverbed and earthen embankments degrading
131 toward the alluvial plain (Fig. 2a,b). Due to the past river digressions, the sediments are
132 characterized by a complex succession of alluvial deposits belonging to the depositional
133 environments of river channel, river embankment, river rout and floodplain.

The local Emilia-Romagna stratigraphic sequence is divided into an upper and a lower sub-sequence. The upper sub-sequence is divided into 8 members, whose youngest two characterize the local stratigraphical succession of the studied area. The Holocene deposits are approximately 20 m thick and formed by sandy-silty deposits of river channel, river embankment, river rout and by clayey-silty deposits of floodplain with frequent lateral heterogeneities. The upper Pleistocene deposits follow beneath with an approximate thickness of 60 m, formed by a multilayering of fine sediments of marsh origin and coarser sediments of river overflowing.

The complex soil layering does not allow an easy reconstruction of the lithological succession, characterized by frequent lateral and vertical variations (Romeo et al., 2015). Due to the complex soil layering, the hydrogeological features are also complex since the ground water table, oscillating within the first 10 m depth, is hosted in a multilayer aquifer. Although there is a correlation between the ground slope and the direction of drainage, their different gradients imply that the ground water depth is maximum below the old riverbed and progressively decreases toward the floodplain, thus implying different stress conditions in the subsoil. A monitoring period of two years, whose data are available thanks to the Emilia region technical offices, highlights that the ground water table oscillations are limited to less than 2 meters, with a shallower depth during the spring and the deepest one at the end of the summer season.

The area is studied by extensive field investigations mainly consisting of penetrometer tests, integrated by boreholes and some dilatometer tests available in several reports and already collected by Papathanassiou et al. (2015). More in particular, the Liquefaction Potential Index (LPI) and Liquefaction Severity Number (LSN) indexes (Iwasaki et al., 1978; Toprak and Holzer, 2003) have been demonstrated to be suitable for detecting the tendency of different subsoil conditions to generate, or not, liquefaction surface manifestations (Giannakogiorgios et

al., 2015). As reported in Papathanassiou et al. (2015), both LSN and LPI allow the identification of local liquefaction-prone conditions at San Carlo when compared to the observed liquefaction effects induced by the 2012 Emilia earthquake (Fig.1a, Table 1). Along the here considered geological cross section (Fig.2b), the resulting LPI values vary from 11.2 up to 25.7 while the LSN values range from 8.2 up to 27.6. According to Papathanassiou et al. (2015), the so resulting correlation classes vary from 3 to 4, identifying a proneness to soil liquefaction from "likely" to "very likely".

On the basis of the available investigations, a geological model of the investigated site is reconstructed (Romeo et al., 2015). Fig. 2c shows a NW-SE geological profile across the San Carlo village running parallel to the old river bed. As many investigations refer to indirect geotechnical tests (cone penetration test and dilatometer test), they have been interpreted with the perspective of highlighting the soil layers susceptible to liquefaction. In the case of penetrometer tests, the soil classification by Robertson (1986, 1990) is adopted, as it has been found to be most consistent with the liquefaction susceptibility. Having sampled the sands ejected during the liquefaction effects, their grain size distribution has been used to identify the Robertson's classes indicating liquefaction susceptibility. More in particular, according to Robertson (1986; 1990), classes 7-8-9 are obtained for liquefiable soils, based on CPTU, and 5-6 based on SCPTU; classes 1-2-3-4-5-6-10 are obtained for not liquefiable soils, based on CPTU, and 1-2-3-4-7-8-9 based on SCPTU. The layers susceptible to liquefaction correspond to the grain size classes of sands, silty sands and sandy silt. Based on this classification, the layers belonging to the liquefiable classes are grouped by depth. Due to the stratigraphic succession of liquefiable soil layers and the resulting confining pressures, we can infer that only the first two surficial layers could have been involved in liquefaction phenomena. The geological model

180 highlights that three different columns could represent the local typical layering: 1) a single-
181 layer of surficial liquefiable soils; 2) a double-layer of thin liquefiable soils; 3) a double-layer
182 with one thick and one thin liquefiable soils.
183 The local log-stratigraphy pointed out that within the first 15 meters below the ground, there are
184 one or two layers of liquefiable soils dating to Holocene and representing soils of river
185 embankment and river rout (Fig. 2c). Another layer of liquefiable soils dating back to
186 Pleistocene is present at depths greater than 20 m below the ground (Fig. 2c). Except for the first
187 surficial layer, the other layers are partially or fully confined by non-liquefiable soils (clays and
188 silty clays).
189 According to the aforementioned cross section, it can be derived that two sandy-silty layers
190 (hereafter named LS1 and LS2 respectively) are present in the San Carlo village area within the
191 first 20 m below the ground level. The first layer (LS1) is a superficial deposit with a thickness
192 varying from about 5 up to 10 m and corresponds partly to the recent alluvial deposits of the
193 Reno River and its tributaries, and partly to the old river banks. The thickness of the second,
194 deeper layer (LS2) is variable and ranges between 1 and 7 m , and this layer can be attributed to
195 more ancient alluvial deposits. More in particular, LS1 level is a continuous layer prone to
196 liquefaction whose thickness has a significant variation due to the topographic irregularities,
197 which can be mainly related to the paleo-morphology of the old river banks. Moreover, due to
198 its stratigraphic location, after the seismic shaking, this layer could dissipate the originated pore
199 water overpressures only from the topographic surface. LS2 level is a more discontinuous layer,
200 whose thickness varies within a few meter range, i.e. probably related to floods from ancient
201 river banks. This level shows a not continuous shape along the transversal sections and, where
202 present, it is separated from the LS1 level by a level not susceptible to liquefaction, having a

thickness varying up to about 6 m. Due to such a stratigraphic setting, the LS2 level can be regarded as a not drained one, i.e. co-seismic drainage of pore water due to overpressures is not possible. Below the LS2 level an about 10 m thick level not susceptible to liquefaction exists, ascribable to the Pleistocene-Holocene; this level rests above a 5 m thick sandy-gravel level (at about -5 m a.s.l., i.e. 20 m b.g.l.), ascribable to the Pleistocene deposits.

Based on the engineering-geological model obtained for the San Carlo village three reference soil columns (C1, C2 and C3 of Fig. 2c) were derived for the 1D numerical modeling, which are summarized below:

- column C1: sandy-silt LS1 and LS2 levels (prone to cyclic mobility and liquefaction) are interlayered with two silty-clayey levels (not susceptible to cyclic mobility and liquefaction) which rest above a sandy-gravel level at about 20 m b.g.l.. This column was obtained by attributing to the silty-clayey level between LS1 and LS2 the lowest assumable thickness (i.e. equal to 2.3 m).
- column C2: sandy-silt LS1 and LS2 levels (prone to cyclic mobility and liquefaction) are interlayered with two silty-clayey levels (not susceptible to cyclic mobility and liquefaction) which rest above a sandy-gravel level at about 20 m b.g.l.. This column was obtained by attributing to the silty-clayey level between LS1 and LS2 the highest assumable thickness (i.e. equal to 5.2 m).
- column C3: a unique sandy-silt LS1+LS2 level prone to liquefaction is considered with the highest assumable thickness (i.e. equal to 12 m).

The safety factor (SF) against liquefaction has been computed for each column by the code CLiq v1.7 (Geologismiki®) according to the method of Robertson & Wride (1998), based on the ratio of demand (cyclic stress ratio) and capacity (cyclic resistance ratio). Only the sandy layers

between 5 and 10 m deep resulted to be liquefiable (SF < 1) in agreement with the results obtained by Facciorusso et al. (2015).

ONE-DIRECTIONAL THREE-COMPONENT WAVE PROPAGATION MODEL

The subsoil is assumed as horizontally layered (as it can be confirmed by the vertical section shown in Fig. 2c) and is modeled as a 1D soil profile (Fig. 3), considering its very large lateral extension. The multilayered soil is assumed infinitely extended along the horizontal directions x and y and, consequently, no strain variation is considered in these directions. A three-component seismic wave propagates vertically in z-direction from the top of the underlying elastic bedrock to the free surface. The soil is assumed to be a continuous medium, with nonlinear constitutive behavior.

The soil profile is discretized, using a finite element scheme, into quadratic line elements having three translational degrees of freedom per node. The finite element model applied in the present research is completely described in Santisi d'Avila et al. (2012).

The subsoil layers are bounded at the bottom by a semi-infinite elastic medium, representing the seismic bedrock. The absorbing boundary condition proposed by Joyner & Chen (1975) is applied at the soil-bedrock interface to take into account the finite rigidity of the bedrock and allows energy to be radiated back into the underlying medium. The bedrock is characterized by the shear and pressure wave velocities in the medium and density. The 3C velocity time histories at the bedrock level are obtained by deconvolution of a seismic signal representative of outcropping bedrock. The soil motion at the soil-bedrock interface, i.e. at the first node of the mesh (Fig. 3), is composed of the incident and reflected waves and it is computed during the process. At this regard, the interested reader can refer to Santisi d'Avila et al. (2012) for more

249 details. As the considered horizontally layered subsoil is bounded at the top by the free surface,
250 the stresses normal to the free surface are assumed to be null.
251 The finite element size in each soil layer is defined as the minimum between 1m and λ/p,
252 where $\lambda = v_{si}/f$, $p = 10$ is the minimum number of nodes per wavelength to accurately
253 represent the seismic signal, v_{si} is the shear wave velocity in the *i*-th soil layer and $f = 15\,\mathrm{Hz}$ is
254 the maximum frequency above which the spectral content of the input signal can be considered
255 negligible. The number of finite elements per layer takes into account the expected reduction of
256 the shear wave velocity v_s, during the dynamic process, that modifies the wavelength $\lambda = v_{si}/f$.
257 The implicit dynamic process is solved step-by-step by Newmark's algorithm. The two
258 parameters $\beta = 0.3025$ and $\gamma = 0.6$ guarantee an unconditional numerical stability of the time
259 integration scheme (Hughes, 1987) and numerical damping, to reduce the not physical high
260 frequency content numerically generated without having any significant effect on the
261 meaningful, lower frequency response. According to Hughes (1987), the numerical damping is
262 about 3% at 10Hz. Moreover, the nonlinearity of soil demands the linearization of the
263 constitutive relationship within each time step. The discrete dynamic equilibrium equation does
264 not require an iterative solving, within each time step, to correct the tangent stiffness matrix, if a
265 small fixed time step $dt = 10^{-4}\,\mathrm{s}$ is selected. Gravity load is imposed as static initial condition in
266 terms of strain and stress.
267

268 **FEATURES OF THE 3D NONLINEAR HYSTERETIC MODEL**

269 The 3D elasto-plastic model for soils used in the presented finite element scheme is inspired
270 from that suggested by Iwan (1967) and applied by Joyner (1975) and Joyner and Chen (1975) in
271 a finite difference formulation, in terms of total stresses.

The adopted model for TSA of soils satisfies the so-called Masing criteria (Kramer, 1996) that does not depend on the number of loading cycles. As a consequence, in a total stress analysis, the effects of the soil nonlinearity could be overestimated reducing the maximum strain values. According to Joyner (1975), the tangent constitutive matrix is deduced from the actual strain level and the strain and stress values at the previous time step. Then, the knowledge of this matrix allows calculating the stress increment. Consequently, the stress level depends on the strain increment and strain history but not on the strain rate. Therefore, this rheological model has no viscous damping. The energy dissipation process is purely hysteretic and does not depend on the frequency.

A correction of mechanical properties is applied according to Iai's model (Iai et al., 1990a,b), for liquefiable soil layers. Iai's rheological model for saturated soils allows attaining larger strains with proper accuracy describing the cyclic mobility process. This correction for liquefiable soils results in a reduction of hysteretic damping overestimation due to the Masing criteria and an increase of the expected maximum strains.

Plasticity model

Iwan's model is a 3D elasto-plastic model with linear kinematic hardening, that allows taking into account the nonlinear hysteretic behavior of soils. Elastic parameters are the shear modulus $G_0 = \rho v_s^2$ (where ρ is the mass density and v_s the shear wave velocity in the medium) and the P-wave modulus $M = \rho v_p^2$ (where v_p is the pressure wave velocity in the medium). The Poisson's ratio ν is related with the compressional to shear wave velocity ratio as $\left(v_p / v_s\right)^2 = 2\left(1-\nu\right)/\left(1-2\nu\right)$.

The 6-dimensional vector of total deviatoric strain rate $\Delta\mathbf{e}$ is written in terms of the elastic and

plastic deviatoric strain rates as $\Delta\mathbf{e} = \Delta\mathbf{e}_E + \Delta\mathbf{e}_P$. The elastic deviatoric strain vector is

$$\Delta\mathbf{e}_E = \mathbf{S}/(2G_0) \tag{1}$$

where $\mathbf{S}$ is the 6-dimensional deviatoric stress vector.

The plasticity model uses von Mises yield surfaces that assume a pressure-independent behavior, namely, yielding is independent of the average pressure stress p. This assumption is acceptable for soils in undrained conditions, as during a sudden seismic event. However, the Iai's correction for effective stress analysis is pressure-dependent.

A family of n yield surfaces is represented by the yield functions

$$F_i(\mathbf{S}-\boldsymbol{\alpha}_i) - \tau_i^2 = 0 \tag{2}$$

where $\boldsymbol{\alpha}_i$ is the kinematic shift of the ith yield surface and $F_i(\mathbf{S}-\boldsymbol{\alpha}_i)$ is the ith von Mises yield surface defined as

$$F_i(\mathbf{S}-\boldsymbol{\alpha}_i) = 1/2(\mathbf{S}-\boldsymbol{\alpha}_i)^T(\mathbf{S}-\boldsymbol{\alpha}_i) \tag{3}$$

The size of the yield surface $\tau_i = \tau_i(e_i)$ is imposed by giving the value of the yield shear stress τ_i, as a function of shear strain e_i, in the case of simple shear.

The kinematic hardening models are used to simulate the inelastic behavior of materials that are subjected to cyclic loading. The linear kinematic model approximates the hardening behavior with a constant rate of hardening, as expressed by the Prager hardening rule

$$\Delta\boldsymbol{\alpha}_i = C_i \Delta\mathbf{e}_{Pi} \tag{4}$$

where C_i are the initial kinematic hardening moduli for each back stress $\boldsymbol{\alpha}_i$, defined as (Joyner, 1975)

$$\frac{1}{C_i} = \frac{e_{i+1} - e_i}{\tau_{i+1} - \tau_i} - \frac{1}{2G} - \sum_{j=1}^{i-1} \frac{1}{C_j} \tag{5}$$

316 The plasticity model assumes an associated plastic flow, which allows for isotropic yield.
317 Therefore, as the material yields, the inelastic deformation rate is in the direction of the normal to
318 the yield surface (the plastic deformation is volume invariant). The rate of plastic flow $\Delta\mathbf{e}_P$ is
319 defined by the following flow rule:

320 $$\Delta\mathbf{e}_{Pi} = L_i \, \Delta\lambda_{Pi} \frac{\partial F_i}{\partial \mathbf{S}} \tag{6}$$

321 The coefficient L_i is defined as

322 $$\begin{aligned} L_i &= 0 \quad \text{for} \quad F_i < \tau_i^2 \quad \text{or} \quad \frac{\partial F_i}{\partial \mathbf{S}} d\mathbf{S} < 0 \\ L_i &= 1 \quad \text{for} \quad F_i = \tau_i^2 \quad \text{and} \quad \frac{\partial F_i}{\partial \mathbf{S}} d\mathbf{S} \geq 0 \end{aligned} \tag{7}$$

323 and $\Delta\lambda_P$ is the plastic strain rate, that is deduced, according to Fung (1965) as

324 $$\Delta\lambda_{Pi} = \frac{1}{C_i} \frac{\dfrac{\partial F_i}{\partial s_{rs}} \Delta S_{rs}}{\dfrac{\partial F_i}{\partial s_{lm}} \dfrac{\partial F_i}{\partial s_{lm}}} \tag{8}$$

325 Consequently, the terms of the plastic deviatoric strain $\Delta\mathbf{e}_{Pi}$ in equation (6) become

326 $$\Delta e_{Pihj} = \left[\sum_{i=1}^{n} L_i \frac{1}{C_i} \frac{\dfrac{\partial F_i}{\partial S_{rs}}}{\dfrac{\partial F_i}{\partial S_{lm}} \dfrac{\partial F_i}{\partial S_{lm}}} \frac{\partial F_i}{\partial S_{hj}} \right] \Delta S_{rs} \tag{9}$$

327 Writing the incremental constitutive relationship as

328 $$\Delta\mathbf{e} = \mathbf{E}_d^{-1} \Delta\mathbf{S} \tag{10}$$

329 and considering equations (1) and (9), the terms of the inverse deviatoric constitutive matrix $\mathbf{E}_d^{-1}$
330 are deduced as

331 $$\frac{1}{2G_0}+\sum_{i=1}^{n} L_i \frac{1}{C_i} \frac{\dfrac{\partial F_i}{\partial S_{rs}}}{\dfrac{\partial F_i}{\partial S_{lm}} \dfrac{\partial F_i}{\partial S_{lm}}} \frac{\partial F_i}{\partial S_{hj}} \tag{11}$$

332 Coefficients in equation (11) are the derivatives of functions F_i in equation (3), that are

333 $$\frac{\partial F_i}{\partial S_{jk}} = \frac{1}{2}\left(S_{jk} - \alpha_{i\,jk}\right) \tag{12}$$

334 When the deviatoric constitutive matrix is known, it is possible to evaluate the deviatoric stress
335 rate as $\Delta\mathbf{S} = \mathbf{E}_d\,\Delta\mathbf{e}$. The (6×6)-dimensional tangent constitutive matrix $\mathbf{E}$, that relates the total
336 stresses and strains in the form $\Delta\boldsymbol{\sigma} = \mathbf{E}\,\Delta\boldsymbol{\varepsilon}$, is obtained from $\mathbf{E}_d$ according to Santisi d'Avila et
337 al. (2012).
338 According to Joyner (1975), to ensure that the stress remains on the yield surface, $\Delta\boldsymbol{\alpha}_i$ is not
339 calculated using equation (4), but the following relationship:

340 $$\boldsymbol{\alpha}_{i\,k+1} = \mathbf{S}_{k+1} - \frac{\tau_i\left(\mathbf{S}_{k+1} - \boldsymbol{\alpha}_{ik}\right)}{\sqrt{1/2\left(\mathbf{S}_{k+1} - \boldsymbol{\alpha}_{ik}\right)^T\left(\mathbf{S}_{k+1} - \boldsymbol{\alpha}_{ik}\right)}} \tag{13}$$

341 The failure curve $\Delta\tau(\gamma) = G(\gamma)\Delta\gamma$, where $G(\gamma)$ is the shear modulus decay curve versus shear
342 strain γ is needed to characterize the soil behavior. The main feature of Iwan's model is that the
343 mechanical parameters to calibrate the rheological model are easily obtained from laboratory
344 dynamic tests on soil samples.
345 The applied constitutive model does not depend on the selected initial loading curve. In the
346 present study, normalized shear modulus decay curves are provided by laboratory tests, as
347 resonant column (RC), and fitted by the function $G(\gamma)/G_0 = 1/\left(1+\left|\gamma/\gamma_{r0}\right|\right)$, where γ_{r0} is a
348 reference shear strain corresponding to an actual tangent shear modulus $G(\gamma)$ equivalent to 50%

of the elastic shear modulus G_0. This model provides a hyperbolic stress-strain curve (Hardin and Drnevich, 1972), having asymptotic shear stress $\tau_0 = G_0 \gamma_{r0}$ in the case of simple shear. If no additional information is available, the normalized compressional modulus reduction curve E/E_0 is assumed equal to the shear modulus reduction curve G/G_0, under the commonly agreed hypothesis of constant Poisson's ratio during the time history.

Correction of mechanical parameters for soils in ESA

Effective stresses follow Terzaghi's law. Note that in the presented formulation the prime indicates effective stresses. The average effective stress is defined as $p' = \left(\sigma'_1 + \sigma'_2 + \sigma'_3\right)/3 = p - u$, where $p = \left(\sigma_1 + \sigma_2 + \sigma_3\right)/3$ is the average total stress, σ_1, σ_2 and σ_3 are the principal stresses and u is the pore water pressure. The initial average effective stress is p'_0. The deviatoric stress is $\tau = \left(\sigma_{\max} - \sigma_{\min}\right)/2 = \tau'$, where $\sigma_{\max}$ and $\sigma_{\min}$ are the maximum and minimum principal stresses, respectively.

The liquefaction front in the plane (r, S) is represented in Fig. 4, where $S = p'/p'_0$ is the state variable, with $0 \le S \le 1$, and $r = \tau/p'_0$ is the deviatoric stress ratio. According to Iai et al. (1990a,b), the state variable S relates the initial and the actual average effective stress and it is expressed as

$$S = \begin{cases} S_0 & r \le r_3 \\ S_2 + \sqrt{\left(S_0 - S_2\right)^2 + \left[\left(r - r_3\right)/m_1\right]^2} & r > r_3 \end{cases} \quad (14)\text{a,b}$$

where $m_1 = \tan\alpha = \sin\phi'$ is the failure line slope (Fig. 4) and ϕ' is the shear friction angle. It can be remarked in Fig. 4 that $\left(r_2 - r_3\right)/\left(S_0 - S_2\right) = m_1$. Accordingly, the parameter S_2 is obtained as

$$S_2 = S_0 - \left(r_2 - r_3\right)/m_1 \tag{15}$$

In equation (15), it is $r_2 = m_2 S_0$, $r_3 = m_3 S_0$, $m_3 = 0.67\, m_2$ and $m_2 = \tan\alpha_p = \sin\phi'_p$ is the phase transition line slope (Fig. 4), where ϕ'_p the phase transformation angle.

The initial value of liquefaction front parameter S_0 is determined by imposing the initial condition $S = 1$ in equation (14)b, according to (15). In dry and non-liquefiable layers, it is $S = 1$ during the seismic event.

Iai et al. (1990a,b) provide a relationship to correlate the liquefaction front parameter S_0 and the normalized shear work w, as follows:

$$\begin{aligned} S_0 &= \left(0.4 - S_1\right)\left(w_1/w\right)^{p_2} + S_1 \quad && w \geq w_1 \\ S_0 &= 1 - 0.6\left(w/w_1\right)^{p_1} && w < w_1,\ S_1 = 1 \end{aligned} \tag{16)a,b}$$

Accordingly, it is

$$\begin{aligned} w &= w_1\left[\left(S_0 - S_1\right)/\left(0.4 - S_1\right)\right]^{-1/p_2} && S_0 \leq 0.4 \\ w &= w_1\left[\left(1 - S_0\right)/0.6\right]^{1/p_1} && S_0 > 0.4 \end{aligned} \tag{17)a,b}$$

The normalized shear work is $w = W_s/W_n$. The normalization factor is $W_n = \left(p'_0\, m_1\right)\gamma_{r0}/2$, where γ_{r0} is the reference strain used in the hyperbolic formulation adopted for the backbone curve. The plastic shear work W_s is unknown at the initial conditions and it is estimated from w (equation (17)) and W_n. The correlation between S_0 and w, in equation (17), depends on four material parameters S_1, w_1, p_1 and p_2 that characterize the liquefaction properties of the cohesionless soil.

The main process starts with the computation of the actual plastic shear work. The increment of plastic shear work at each time step is

388 $$dW_s = R\left(dW_{st} - c_1\, dW_{se}\right) \geq 0 \qquad (18)a,b$$

389 where, according to Towhata and Ishihara (1985), the shear stress work dW_{st} is evaluated as
390 difference between the total work $dW = \sigma'_{ij}\, d\varepsilon_{ij}$ and the consolidation work $dW_c = p' d\varepsilon_v$, where
391 $d\varepsilon_v$ is the volumetric strain. There exists a threshold limit in the amplitude of cyclic shear strain
392 or shear stress. There is no pore water pressure build-up for cyclic strain or stress below this
393 threshold level. The shear work consumed by the threshold limit is subtracted from the total
394 shear work. It is closely related with the elastic shear work $dW_{se} = \left|\tau\, d\left(\tau/G\right)\right|$. The parameter
395 $c_1 \approx 1$ is introduced to correct the elastic shear work dW_{se} for the purpose of obtaining the shear
396 work consumed by the threshold limit. R is a correction factor for dW_s in the case of dilatancy,
397 that means $\tau > p_0\, m_2$, and $r/S > m_3$. It is defined as

398 $$\begin{aligned} R &= \left(m_1 - r/0.4\right)/\left(m_1 - m_3\right) \quad S_0 \leq 0.4 \\ R &= \left(m_1 - r/S\right)/\left(m_1 - m_3\right) \quad S_0 > 0.4 \end{aligned} \qquad (19)a,b$$

399 When the actual plastic shear work W_s is known, the normalized shear work w is evaluated, the
400 liquefaction front parameter S_0 is deduced from equation (16) and the state variable S is
401 obtained by equation (14). According to the definition of S, the actual average effective stress
402 $p' = S\, p'_0$ and the increment of water pressure $\Delta u = p'_0 - p' > 0$ are obtained during the time
403 history. The actual effective stress $\sigma' = \sigma - u$ is deduced from the total stress and water pressure
404 $u = p - p'$. Finally, the updated deviatoric stress τ_a and the reference shear strain γ_{ra} are
405 estimated as

406 $$\begin{aligned} \tau_a &= \tau_0\, S & \gamma_{ra} &= \gamma_{r0} & S_0 > 0.4 \\ \tau_a &= \tau_0\, S + \Delta\tau = \tau_0\, S + \tau_0\left(1 - m_1/m_2\right)\left(0.4 - S_0\right) & \gamma_{ra} &= \gamma_{r0}/\left(S_0/0.4\right) & S_0 < 0.4 \end{aligned} \qquad (20)a,b$$

The corrected shear modulus is

$$G_a = \tau_a / \gamma_{ra} \tag{21}$$

Consequently, the normalized shear modulus decay curve is updated as $G(\gamma)/G_a = 1/(1+|\gamma/\gamma_{ra}|)$.

Characterization of soil parameters in ESA

Seven parameters have to be fixed to calibrate Iai's correction of shear modulus of soils for ESA. They are the shear friction angle ϕ', the phase transformation angle ϕ'_p, the parameter c_1 that corrects the elastic shear work and the four parameters S_1, w_1, p_1 and p_2 that influence the relationship between the liquefaction front parameter S_0 and the normalized shear work w.

The shear friction angle ϕ' and the phase transformation angle ϕ'_p are obtained from static Consolidated Undrained (CU) triaxial tests, using the (τ, p') curve for three different confining pressure levels. The slope of the line connecting the rupture points, for the three different confining pressure levels, is the trigonometric tangent of angle α. The slope of the line connecting the inflection points of the three curves is the trigonometric tangent of angle α_p. The shear friction angle ϕ' and the phase transformation angle ϕ'_p are obtained considering the equivalences $\tan\alpha = \sin\phi'$ and $\tan\alpha_p = \sin\phi'_p$, respectively.

According to Iai et al., 1990a,b, parameters S_1, w_1, p_1 and p_2 are deduced from CTX tests. Three curves have to be reproduced: the cyclic deviatoric stress, the deviatoric strain amplitude and the normalized excess pore water pressure $\Delta u/p'_0$ with respect to the number of cyclic loading N, where $\Delta u = p'_0 - p'$ is the excess pore water pressure.

MODEL OF SELECTED SOIL PROFILES

The definition of the three analyzed soil profiles, named here C1, C2 and C3, is derived from the stratigraphy in the San Carlo area, at about 17 km from the epicenter of the 2012 Emilia earthquake. The selected stratigraphy for the three columns C1, C2 and C3, and the mechanical parameters identified for each layer are presented in Tables 2, 3 and 4, respectively. The front liquefaction parameters are also reported for cohesionless soil layers, subjected to possible cyclic mobility effects and liquefaction phenomena. Liquefiable soil layers are the 1st, 3rd and 5th in soil columns C1 and C2, and the 1st and 3rd in C3.

An in-situ test using seismic dilatometer has been used to obtain profiles with depth of the shear wave velocity v_s, total (wet) density ρ and at-rest lateral earth pressure coefficient K_0. The initial elastic shear modulus G_0 is evaluated as $G_0 = \rho v_s^2$. The elastic P-wave modulus is evaluated as $M_0 = \rho v_p^2$, where the compressional wave velocity v_p is deduced from the relationship $v_p = v_s \sqrt{2(1-\nu)(1-2\nu)}$, where the Poisson's ratio is obtained as $\nu = K_0/(1+K_0)$.

Laboratory tests are used to obtain the mechanical features of each soil layer, useful to define the initial conditions in the numerical simulation. A RC test gives the normalized shear modulus reduction curve $G(\gamma)/G_0$ that is fitted using a curve corresponding to a hyperbolic stress-strain curve. The reference shear strain γ_{r0} is deduced as the strain corresponding to $G = 0.5 G_0$. The shear modulus reduction curves obtained by laboratory data are given in Table 5, for the soil samples used to characterize the analyzed soil columns. The normalized curves, fitted by the hyperbolic model are shown in Fig. 5.

The variation of the elastic shear modulus with depth is taken into account for the liquefiable

soil layers. It is corrected according to $G_0(z) = G_0(z_m)\, p'_0(z) / p'_0(z_m)$, where p'_0 is the average pressure, z_m is the depth at the middle of the layer and $G_0(z_m) = \rho v_s^2$ is calculated using the values of density and shear velocity reported in Tables 2-4 for each soil layer. As consequence, the shear strength $\tau_0 = G_0 \gamma_{r0}$ is modified. In non-liquefiable layers, considering that their thickness is limited, the shear modulus is assumed constant with depth.

A CU triaxial test provides the shear friction angle ϕ' and the phase transformation angle ϕ'_p using a curve (τ, p') for three different confining pressure levels. The slope of the line connecting the rupture points, for the three different confining pressure levels, is the trigonometric tangent of the shear friction angle ϕ'. The slope of the line connecting the inflection points of the three curves is the trigonometric tangent of the phase transformation angle ϕ'_p.

The CTX test gives the liquefaction front parameters c_1, S_1, w_1, p_1 and p_2 as explained in the next subsection.

The average effective stress in geostatic conditions $p'_0 = (\sigma'_v + 2\sigma'_h)/3$ is evaluated considering the vertical effective stress $\sigma'_v(z) = \rho g z - u_0(z)$, variable with depth z (g is the gravitational acceleration) and dependent on the initial pore water pressure $u_0(z)$, and the horizontal effective stresses estimated as $\sigma'_h(z) = K_0 \sigma'_v(z)$. At the surface, where the vertical stress attains zero but the confinement, even if reduced, is not annulled, the horizontal effective stresses are corrected and assumed equal to $\sigma'_h = K_0 \sigma'_v(z_p)$ in the first z_p meters (in this study, it is assumed $z_p = 5\,\mathrm{m}$).

Fitting of cyclic consolidated undrained triaxial test curves

The parameters S_1, w_1, p_1 and p_2 are deduced from CTX tests. The cyclic deviatoric stress (total axial stress minus confining pressure) produced during the test is used to estimate the total axial stress that is adopted as input in a numerical simulation, known the cell pressure $p_0 = 300\,\mathrm{kN/m^2}$ and the back pressure $u_0 = 200\,\mathrm{kN/m^2}$ during the test. The axial deviatoric strain amplitude and the normalized excess pore water pressure $\Delta u / p_0'$ ($\Delta u = p_0' - p'$ is the excess pore water pressure), with respect to the number of cyclic loading N, are obtained numerically and compared to the two curves produced during the test.

In order to obtain numerically the curves that best reproduce the experimental ones, the parameters w_1 and p_1 are determined by a trial-and-error procedure, to obtain a normalized excess pore water pressure curve that best reproduce the experimental curve in the portion of the curve for $\Delta u / p_0' < 0.6$. The parameter w_1 is not greatly influenced by the variation of p_1, so it is determined at first for a given value of p_1. The appropriate value of p_1 is researched in the interval $[0.4 - 0.7]$, according to Iai et al. (1990b). The greater w_1 and p_1 are, the slower the pore water pressure rises. The envelope of strain amplitude is also fitted, observing that the greater w_1 is, the more it reduces the envelope of strain amplitude.

The parameter p_2 is researched in the interval $[0.6 - 1.5]$ (Iai et al. 1990b). It is determined as well by a trial-and-error process, to obtain a normalized excess pore water pressure curve that best fit the experimental curve in the portion of the curve for $\Delta u / p_0' > 0.6$. Since the curve is not greatly influenced by the variation of p_2, the envelope of strain amplitude is also fitted. The greater p_2 is, the more it increases the envelope of strain amplitude.

According to Iai et al. (1990b), the parameter $S_1 \geq 0.005$ is introduced so that S_0 will never be zero. It takes small positive values, determined by the trial-and-error procedure to obtain the best fit of the experimental normalized excess pore water pressure curve. The analyzed tests appear not sensitive to a variation of S_1. The first trial is maintained for all the layers: $S_1 = 0.005$. The parameter c_1 is imposed equal to one when w_1, p_1 and p_2 are determined and, if laboratory data are not well represented in the elastic range, c_1 can be modified using a trial-and-error procedure. The mechanical parameters measured by laboratory tests (RC, CU) are listed in Table 6 for the analyzed soil samples S11-C1 (associated to the liquefiable layer LS1 in Tables 2-4) and S11-C3 (associated to LS2). The selected liquefaction parameters for S11-C1 and S11-C3 are the average between the values obtained by calibration for the two available tests (listed in Table 6) and these selected values are assumed constant with depth within each liquefiable soil layer. The fitting of CTX test curves is shown in Fig. 6 for the S11-C1-2 soil sample (see Table 6) and in Fig. 7 for the S11-C1-3 soil sample. Figs 6 and 7 show the measured cyclic axial deviatoric stress, applied as input, the measured and numerical axial deviatoric strain amplitude and normalized excess pore water pressure with respect to the number of cyclic loading. The curves (τ, p') and (r, S) are evaluated numerically.

Input seismic motion

Since in May 2012 the stations of the fixed Italian National Accelerometric Network (RAN) were not present in the municipal area of San Carlo, the mainshock was not recorded in this site. Even though the temporary array, installed the day after the mainshock by the Nacional Civil Protection, recorded 12 seismic events with M_w higher than 4, no further liquefaction effects have been observed after the mainshock of 20 May 2012. Therefore, as reported by Romeo et al.

515 (2015), the seismic input at the San Carlo site was derived by: 1) evaluating a spectrum of
516 scenario for the site of San Carlo; 2) selecting the record of the 20 May 2012 mainshock at
517 Mirandola as reference input and deconvolving it to bedrock and outcrop; 3) attenuating the
518 record of Mirandola at the outcropping bedrock of San Carlo using the ground motion prediction
519 equation proposed by Sabetta and Pugliese (1987).
520 The three-components of the reference outcropping motion are halved and applied as incident
521 wavefield at the base of the analyzed soil columns.
522 The reference incident motion applied at the soil-bedrock interface is shown in Fig. 8, in terms of
523 acceleration. The peak acceleration is 2.54 $\mathrm{m/s^2}$ in North-South direction (named *x* in the
524 model), 1.51 $\mathrm{m/s^2}$ in East-West direction (named *y*) and 0.33 $\mathrm{m/s^2}$ in Up-Down direction
525 (named *z*).
526 All input and output signals are filtered using a 4-pole Butterworth bandpass filter in the
527 frequency range $0.1-15\,\mathrm{Hz}$.
528
529 **EEFECT OF WATER TABLE DEPTH VARIATION**
530 First, the seismic response of the analyzed soil profiles to the 20 May 2012 Mw 5.9 Emilia
531 earthquake is estimated in terms of total stresses, to assess the extent of error in this study case
532 where liquefaction phenomena are expected. Then, the analysis is developed in terms of effective
533 stresses.
534 The assumed water table depth is $z_w = 5.8\,\mathrm{m}$ for C1 column, $z_w = 5.2\,\mathrm{m}$ for C2 column and
535 $z_w = 2.7\,\mathrm{m}$ for C3 column, according to the available technical reports. Moreover, a water table
536 variation of $\pm 1\mathrm{m}$ is considered in this research and its influence on the soil column response to
537 the seismic loading is analyzed.

538 Profiles with depth of the peak acceleration and velocity, shear strain and stress for the soil
539 profile C1 are represented in Fig. 9, in the cases of TSA and ESA with variable water table
540 position. Strains are increased in liquefiable layers, compared with the TSA assumption. The
541 shape of loops in liquefiable soil layers is influenced by the reduction of shear modulus during
542 the cyclic mobility (Fig. 10 bottom). Profiles with depth and hysteresis loops for soil columns C2
543 and C3 are presented in Figs 11-12 and 13-14, respectively.
544 In liquefiable soil layers, the shear modulus is reduced during the cyclic mobility and the
545 reference shear strain γ_{r0} is numerically corrected when the liquefaction front parameter S_0 is
546 lower than 0.4, according to Equation (20). The minimum values attained by the shear modulus
547 during the process, at each depth, and the maximum reference shear strain are shown in Fig. 15,
548 for the C3 soil profile.
549 Observing Figs 9-14, the considered variation of the water table position equal to $\pm 1\text{m}$ is not
550 influent in the seismic response of the analyzed soil profiles. In the analyzed case study, a total
551 stress analysis, for a stratigraphy where there are liquefiable soil layers, totally modifies the
552 seismic response, neglecting the reduction of soil stiffness and the increase of ground motion.
553 According to Figs 9, 11, 13, 16 and 17 and Table 7, the TSA assumption underestimates the peak
554 values of motion.
555 According to Figs 9, 11 and 13, the maximum shear strain level, estimated using the analysis in
556 terms of effective stress, is 6.8%, 5.6% and 6.2% for C1, C2 and C3 soil profiles, respectively.
557 Maximum acceleration profiles with depth are obtained during the process using unfiltered
558 acceleration. Figs 16-17 show filtered horizontal acceleration at the ground surface. The
559 variability in the peak ground acceleration with the water table position is negligible (see Table
560 7).

561 The expected level of horizontal peak ground acceleration, corresponding to about 0.32 g
562 according to the automated shakemaps (INGV, see Data and Resources), is numerically obtained
563 for the C3 soil profile (Table 7).
564 Fig. 18a shows the profiles with depth of maximum excess pore water pressure, normalized with
565 respect to the initial average effective pressure, for the three analyzed soil columns. The
566 maximum excess pore water pressure attains 84%, 93% and 98% of the initial average
567 effective pressure, respectively. The time history at the depth where the excess pore water
568 pressure attains the maximum value is shown in Fig. 18b.
569

570 **CONCLUSIONS**

571 A one-directional propagation model of a three-component seismic wave (1D-3C approach), in a
572 finite element scheme, is used to investigate the seismic response and stress-strain induced
573 effects of three soil profiles derived from the stratigraphy of San Carlo village (Emilia Romagna,
574 Italy). A representative record for the 20 May 2012 Mw 5.9 Emilia earthquake is applied as input
575 motion at the soil-bedrock interface.
576 During the 20 May 2012 Mw 5.9 Emilia earthquake, liquefaction phenomena have been
577 observed. Consequently, an analysis in terms of total stresses is not suitable. A constitutive
578 behavior based on soil plasticity with hardening (Iwan's model) is used, where the nonlinearity is
579 described by the normalized shear modulus reduction curve. The shear modulus is corrected
580 during the process, depending on the actual average effective stress (Iai's model) to consider the
581 cyclic mobility and dilatancy of sands.
582 The seismic response of the analyzed soil profiles is discussed in terms of profiles with depth of
583 maximum shear strain and stress, peak of the horizontal motion and maximum excess pore water

584 pressure. Hysteresis loops in liquefiable soils and the time histories of the ground motion and the
585 excess pore water pressure are obtained for the different hypothesis of the water table depth.
586 The impact of ESA soil modeling in the numerical seismic response of a soil profile, compared
587 with a total stress analysis, is observed for the analyzed case study and shows that the TSA
588 assumption underestimates the peak values of the ground motion.
589 The influence on the numerical seismic response and the stress-strain effects of the water table
590 depth variability is investigated and it appears negligible in the analyzed case study.
591 The attained maximum shear strain level, estimated using nonlinear analysis in terms of effective
592 stress, attains 6%, confirming the observed liquefaction effect. The expected level of horizontal
593 peak ground acceleration, deduced from the automated shakemaps, is numerically reproduced.
594 The maximum excess pore water pressure, obtained numerically, attains 98% of the initial
595 average effective pressure in C3 soil profile.
596 The discrepancy between geotechnical parameters, obtained by different in-situ and laboratory
597 tests, forces to some modeling choices. Further experimental research should be necessary to
598 guarantee the interdependence of geotechnical data issued by tests for different soil samples in
599 the same area and to regulate the procedure allowing the transposition of measures in the
600 modeled soil profile.
601 The numerical approach applied here can be regarded as a useful tool for identifying subsoil
602 portion prone to soil liquefaction during earthquakes. This allows the outline of unstable zones
603 for expected nonlinear effects in the framework of Seismic Microzonazion Studies. In this
604 regard, high resolution engineering-geological modeling of the subsoil makes it possible to
605 extend the local numerical results (i.e. output from a single soil column) to adjacent areas, based
606 on the similarity of soil layering and hydrogeological conditions. Such an approach exemplifies

607 the efficiency of a multidisciplinary approach which merges geological, physical and engineer
608 features to quantify complex effects involving a multiphase rheological system.
609
610 **DATA AND RESOURCES**
611 Seismograms and soil stratigraphic setting used in this study were obtained in the framework of
612 the Project S_2-2012 by INGV-DPC 2012-2013 – UR4 titled: "Validation of Seismic Hazard
613 through observed data; Constraining OBservations into Seismic hazard (COBAS)" (scientific
614 responsible: Laura Peruzza; UR4 co-ordinator R.W. Romeo**)**. The laboratory tests used for this
615 study were performed on commission by the C.G.G. Testing S.r.l. laboratory of Bologna (Italy).
616 The Italian catalogue of earthquake-induced ground effects (CEDIT) is available online at the
617 URL http://www.ceri.uniroma1.it/index_cedit.html (last accessed November 2017).
618 Shakemaps produced by the Italian National Institute of Geophysics and Volcanology (INGV)
619 are available online at the URL http://shakemap.rm.ingv.it/shake/index.html (last accessed
620 November 2017).
621
622 **ACKNOWLEDGMENTS**
623 The Authors wish to thank the Servizio Geologico della Regione Emilia technical office for the
624 availability of technical data and reports and Carolina Fortunato for her contribution to the
625 reconstruction of the engineering-geological model in the framework of the COBAS project.
626
627 **REFERENCES**
628 Bonilla, L.F., R.J. Archuleta and D. Lavallée (2005). Hysteretic and dilatant behavior of
629 cohesionless soils and their effects on nonlinear site response: field data observations and

630 modeling, *Bull. Seism. Soc. Am.*, 95(6), 2373–2395.

631 Bondesan, M. (1990). L'area deltizia padana: caratteri geografici e geomorfologici, *Il Parco del*
632 *Delta del Po, studi e immagini*, vol. 1, L'ambiente come risorsa, Spazio Libri Editori, Ferrara,
633 10–48.

634 Bondesan, M. (2001). L'evoluzione idrografica e ambientale della pianura ferrarese negli ultimi
635 3000 anni, *Storia di Ferrara*, vol. 1, Territorio e preistoria, Corbo Editori, Ferrara, 228–263.

636 Caputo, R., A. Pellegrinelli, C. Bignami, A. Bondesane, A. Mantovani, S. Stramondo and P.
637 Russo (2015). High-precision levelling, DInSAR and geomorphological effects in the Emilia
638 2012 epicentral area, *Geomorphology*, **235**, 106–117.

639 Chini, M., M. Albano, M. Saroli, L. Pulvirenti, M. Moro, C. Bignami, E. Falcucci, S. Gori, G.
640 Modoni, N. Pierdicca and S. Stramondo (2015). Coseismic liquefaction phenomenon analysis by
641 COSMO-SkyMed: 2012 Emilia (Italy) earthquake. *Int. J. Appl. Earth Obs. Geoinf.*, **39**, 1–14.

642 Chung, J.W., and J.D. Rogers (2013). Influence of Assumed Groundwater Depth on Mapping
643 Liquefaction Potential. *Environmental & Engineering Geoscience*, **19**(4), 377–389.

644 DPC-CRP - Dipartimento della Protezione Civile e Conferenza delle Regioni e delle Province
645 Autonome (2008). Indirizzi e Criteri per la Microzonazione Sismica; Dipartimento della
646 Protezione Civile: Rome, Italy. http://www.protezionecivile.gov.it/jcms/it/view_pub.wp?content
647 Id=PUB1137.

648 Emergeo Working Group (2012). Liquefaction phenomena associated with the Emilia
649 earthquake sequence of May–June 2012 (Northern Italy). *Nat. Hazards Earth Syst. Sci.*, **13**,
650 935–947.

651 Facciorusso, J., C. Madiai and G. Vannucchi (2014). Soil liquefaction analyses in a test-area

affected by the 2012 Emilia-Romagna earthquake (Italy), *Engineering Geology for Society and Territory*, vol. 5, Springer, 1111–1114.

Facciorusso, J., C. Madiai and G. Vannucchi (2015). CPT-based liquefaction case history from the 2012 Emilia earthquake in Italy, *J. Geotech. Geoenviron. Eng.*, **141**(12), 1032–1051.

Fung, Y. C. (1965). *Foundation of soil mechanics*, Prentice Hall, Englewood Cliffs, New Jersey.

Giannakogiorgos, A., G.Papathanassiou and E. Vautherin (2015). Quantitative assessment of liquefaction potential in selected areas in Christchurch, New Zealand. Proc. 6th International Conference on Earthquake Geotechnical Engineering 1-4 November 2015 Christchurch, New Zealand, 1-8.

Hardin, B.O., and V.P. Drnevich (1972). Shear modulus and damping in soil: design equations and curves, *J. Soil Mech. Found. Div.*, **98**, 667–692.

Hartantyo, E., S.K., Brotopuspito, Sismanto, Waluyo (2014). Correlation of shallow groundwater levels with the liquefaction occurrence cause by May 2006 earthquake in the south volcanic-clastic sediments Yogyakarta, Indonesia. *Int. J. of Applied Sciences*, **5**(1), 1–8.

Hughes, T.J.R. (1987). *The finite element method - Linear static and dynamic finite element analysis*, Prentice Hall, Englewood Cliffs, New Jersey.

Iai, S., Y. Matsunaga and T. Kameoka (1990a). *Parameter identification for a cyclic mobility mode*, Report of the Port and harbour Research Institute, **29**(4), 27–56.

Iai, S., Y. Matsunaga and T. Kameoka (1990b). *Strain space plasticity model for cyclic mobility*, Report of the Port and harbour Research Institute, **29**(4), 57–83.

Iwan, W.D. (1967). On a class of models for the yielding behavior of continuous and composite systems, *J. Appl. Mech.*, **34**, 612–617.

674 Iwasaki, T., F. Tatsuoka, K.I. Tokia and S. Yasuda (1978). A practical method for assessing soil
675 liquefaction potential based on case studies at various sites in Japan. 2nd Int. Conf. on
676 Microzonation, San Francisco, Proceedings, pp. 885–896.

677 Nishiwaki, K., Yasuhara, K., Komine, H. and S. Murakami (2009). Displacement and
678 countermeasures for existing structure with rising groundwater levels, Proc. 8th Japan National
679 Symposium on Environmental Geotechnology, pp. 381–384 (Japanese).

680 Joyner, W. (1975). A method for calculating nonlinear seismic response in two dimensions,
681 *Bull. Seism. Soc. Am.*, **65**(5), 1337–1357.

682 Joyner, W.B., and A.T.F. Chen (1975). Calculation of nonlinear ground response in earthquakes,
683 *Bull. Seism. Soc. Am.*, **65**(5), 1315–1336.

684 Kramer, S.L. (1996). *Geotechnical earthquake engineering*, Prentice Hall, New Jersey.

685 Martino, S., A. Prestininzi and R.W. Romeo (2014). Earthquake-induced ground failures in Italy
686 from a reviewed database. *Nat. Hazards Earth Syst. Sci.*, **14**, 799–1814.

687 Papathanassiou, G., A. Mantovani, G. Tarabusi, D. Rapti and R. Caputo (2015). Assessment of
688 liquefaction potential for two liquefaction prone areas considering the May 20, 2012 Emilia
689 (Italy) earthquake, *Engineering Geology*, **189**, 1–16.

690 Régnier, J. *et al*., 2018. PRENOLIN: international benchmark on 1D nonlinear site response
691 analysis - Validation phase exercise. *Bull. Seism. Soc. Am*., 108(2).

692 Robertson, P.K., and C.E. Wride (1998). Evaluating cyclic liquefaction potential using the cone
693 penetration test, *Can. Geotech. J.*, **35**, 442–459.

694 Robertson, P.K. (1986). In situ testing and its application to foundation engineering, *Can.*
695 *Geotech. J.*, **23**, 573–594.

696 Robertson, P.K. (1990). Soil classification using the cone penetration test, *Can. Geotech. J.*,
697 **27**(1), 151–158.
698 Romeo, R.W., S. Amoroso, J. Facciorusso, L. Lenti, C. Madiai, S. Martino, P. Monaco, D.
699 Rinaldis and F. Totani (2015). Soil liquefaction during the Emilia, 2012 seismic sequence:
700 investigation and analysis, In G. Lollino et al. (eds.), Engineering Geology for Society and
701 Territory, vol.5, 1107-1110.
702 Sabetta, F., and A. Pugliese (1987). Attenuation of peak horizontal acceleration and velocity
703 from Italian strong-motion records. *Bull. Seism. Soc. Am.*, **77**, 1491–1513.
704 Santisi d'Avila, M.P., L. Lenti, and J.F. Semblat (2012). Modeling strong seismic ground
705 motion: 3D loading path vs wavefield polarization, *Geophys. J. Int.*, **190**, 1607–1624.
706 Santisi d'Avila, M.P., Viet Anh Pham, L. Lenti, J.F. Semblat (2018). Extended Iwan-Iai
707 constitutive model for 1-Directional 3-Component seismic waves in liquefiable soils: application
708 to the Kushiro site (Japan), *Geophys. J. Int.*, in press.
709 Scognamiglio, L., L. Margheriti, F.M. Mele, E. Tinti, A. Bono, P. De Gori, V. Lauciani, F.P.
710 Lucente, A.G. Mandiello, C. Marcocci, S. Mazza, S. Pintore and M. Quintiliani (2012). The
711 2012 Pianura Padana Emiliana seimic sequence: locations, moment tensors and magnitudes,
712 *Annals of Geophysics*, **55**(4), 549–559.
713 Toprak, S., and T.L. Holzer (2003). Liquefaction potential index: field assessment. *J. Geotech.*
714 *Geoenviron. Eng.*, **129** (4), 315–322.
715 Towhata, I., and Ishihara K. (1985). Shear work and pore water pressure in undrained shear.
716 *Soils and foundations*, **25**(3), 73–84.
717 Vannucchi, G., T. Crespellani, J. Facciorusso, A. Ghinelli, C. Madiai, A. Puliti and S. Renzi
718 (2012). Soil liquefaction phenomena observed in recent seismic events in Emilia-Romagna

719 Region (Italy), *Ingegneria sismica*, vol. 2–3, Pàtron Editore, Bologna.
720 Yasuda, S., and K. Ishikawa (2015). Effect of lowering the ground water table as the
721 countermeasure against liquefaction-induced damage to houses. Journal of Japan Association for
722 Earthquake Engineering, **15**(7), 205-219.
723 Wang, C.Y., D.S Dreger, Wang C.H., Mayeri D. and J.G. Berryman (2003). Field relations
724 among coseismic ground motion, water level change and liquefaction for the 1999 Chi-Chi
725 (Mw=7.5) earthquake, Taiwan. *Geophysical Research Letters*, **30**(17), HLS1-4.
726 Wayne, A.C., and D. O. Doehring (2007). Groundwater table mounding, pore pressure, and
727 liquefaction induced by explosions: energy-distance relations. *Reviews of Geophysics*, **45**,
728 RG4006/2007, 1 of 9. Paper number 2006RG000205.
729

730 **LIST OF FIGURE CAPTIONS**

731 **Figure 1.** Liquefaction effects observed at San Carlo village after the 20 May 2012 M_w 5.9
732 earthquake: a, b) evidences of clay spread out on free field; c, d) evidence of clays spread out
733 from building foundations causing damage to structures.

734 **Figure 2.** (a) Google Earth satellite view of the San Carlo village with trace of geological cross
735 section and location of modelled soil columns. (b) geological map of the San Carlo village: 1)
736 deposits of river channel; 2) deposits of river banks; 3) deposits of alluvial plain; 4) liquefaction
737 sand boil; 5) liquefaction trench; 6) borehole with samples; 7) borehole without samples; 8)
738 Seismic DilatoMeter Test (SDMT); 9) Cone Penetration Test with piezocone (CPTU); 10)
739 Seismic Cone Penetrometric Test with piezocone (SCPTU); 11) Seismic Cone Penetrometric
740 Test (SCPT). (c) Geological cross section: 1) Holocene liquefiable deposits; 2) Holocene not
741 liquefiable deposits; 3) Pleistocene liquefiable deposits; 4) Pleistocene non liquefiable deposits;
742 5) not classified Pleistocene deposits; 6) water table; 7) liquefaction sand boil; 8) liquefaction
743 trench; 9) borehole; 10) CPTU or SCPT test; 11) modelled soil columns.

744 **Figure 3.** Spatial discretization of a horizontally layered soil. The seismic loading applied at the
745 bedrock level is a deconvolved outcropping signal in terms of velocity.

746 **Figure 4.** Liquefaction front $r(S)$, where r is the deviatoric stress ratio and S is the state
747 variable.

748 **Figure 5.** Normalized shear modulus reduction curves obtained using RC test results (markers)
749 and fitted using the hyperbolic model (solid line), for soil samples S2-C2 (left) having reference
750 shear strain $\gamma_{r0} = 0.48‰$, S3-C3 (middle) having $\gamma_{r0} = 0.39‰$ and S10-C3 (right) having
751 $\gamma_{r0} = 0.49‰$.

752 **Figure 6.** Fitting of cyclic Consolidated Undrained triaxial test curves to calibrate liquefaction

753 parameters, for S11-C1-2 soil sample in LS1 liquefiable soil layer.

754 **Figure 7.** Fitting of cyclic Consolidated Undrained triaxial test curves to calibrate liquefaction
755 parameters, for S11-C3-3 soil sample in LS2 liquefiable soil layer.

756 **Figure 8.** Three components of the incident motion applied at the soil-bedrock interface in terms
757 of acceleration. The peak acceleration is 2.54 $\mathrm{m/s^2}$ in *x* -direction, 1.51 $\mathrm{m/s^2}$ in *y*-direction and
758 0.33 $\mathrm{m/s^2}$ in *z*-direction.

759 **Figure 9.** Profiles with depth of maximum shear strain and stress, horizontal velocity and
760 acceleration, during the seismic event, for different water table depth and for TSA conditions in
761 the C1 soil column. The horizontal dashed lines indicate the depth where the shear stress-strain
762 loops are analyzed.

763 **Figure 10.** Hysteresis loops in C1 soil profile for different water table depth and for TSA
764 conditions: (top) at 21.5 m in a non liquefiable soil layer; (bottom) at 13 m in LS2 liquefiable
765 soil layer.

766 **Figure 11.** Profiles with depth of maximum shear strain and stress, horizontal velocity and
767 acceleration, during the seismic event, for different water table depth and for TSA conditions in
768 the C2 soil column. The horizontal dashed lines indicate the depth where the shear stress-strain
769 loops are analyzed.

770 **Figure 12.** Hysteresis loops in C2 soil profile for different water table depth and for TSA
771 conditions: at 9 m (top) and at 12.5 m (bottom) in LS2 liquefiable soil layer.

772 **Figure 13.** Profiles with depth of maximum shear strain and stress, horizontal velocity and
773 acceleration, during the seismic event, for different water table depth and for TSA conditions in
774 the C3 soil column. The horizontal dashed lines indicate the depth where the shear stress-strain
775 loops are analyzed.

776 **Figure 14.** Hysteresis loops in C3 soil profile for different water table depth and for TSA
777 conditions: (top) at 20.5 m in a non liquefiable soil layer; (bottom) at 12 m in LS1+LS2
778 liquefiable soil layer.
779 **Figure 15.** Profile with depth of minimum shear modulus (left), during the seismic event, with
780 zoom in the first soil layers (middle) and profile with depth of the maximum reference shear
781 strain, for different water table depth and for TSA conditions, in the C3 soil profile. The
782 horizontal dashed lines indicate the depth where the shear stress-strain loops are analyzed.
783 **Figure 16.** Acceleration time history at the ground surface for C1 (left), C2 (middle) and C3
784 (right) soil profiles, in *x*-direction, for different water table depth and for TSA conditions.
785 **Figure 17.** Acceleration time history at the ground surface for C1 (left), C2 (middle) and C3
786 (right) soil profiles, in *y*-direction, for different water table depth and for TSA conditions.
787 **Figure 18.** Excess pore water pressure, normalized with respect to the average effective pressure,
788 for different water table depth, in C1 (left), C2 (middle) and C3 (right) soil columns: (top)
789 Profiles with depth of maximum value during the seismic event. The horizontal dashed lines
790 indicate the depth where the time histories are analyzed. (bottom) Time history: at 21.5 m (LS1)
791 in C1 soil profile, at 20.5 m (LS2) in C2 soil profile and at 4.5 m (LS1+LS2) in C3 soil profile,
792 for $z_w = 3.7\,\mathrm{m}$, at 3.5 m for $z_w = 2.7\,\mathrm{m}$ and $z_w = 1.7\,\mathrm{m}$.
793

AUTHORS' AFFILIATION

Maria Paola Santisi d'Avila

Université Côte d'Azur

Laboratoire Jean Alexandre Dieudonné (LJAD)

28 Avenue Valrose, 06108 Nice, France

msantisi@unice.fr

Salvatore Martino

Università Roma "Sapienza"

Dipartimento di Scienze della Terra e Centro di Ricerca per i Rischi geologici (CERI)

Piazzale Aldo Moro, 5, 00185 Roma, Italy

salvatore.martino@uniroma1.it

Luca Lenti

IFSTTAR, Université Paris-Est

14-20 Boulevard Newton, 77447 Champs sur Marne, France

luca.lenti@ifsttar.fr

Roberto Walter Romeo

Libera Università di Urbino Carlo Bo

Via Aurelio Saffi, 2, 61029 Urbino, Italy

roberto.romeo@uniurb.it

TABLES

Table 1. Values of LPI and LSN referred to the SCPTU and CPTU tests located in Fig. 2a and related correlation classes for proneness to soil liquefaction according to Papathanassiou et al., 2015: class-I: “almost no”, class-II: “few”, class-III: “likely” and class-IV: “very likely”.

In-situ test position	LPI	LSN	Correlation class
SCPTU1	25.7	25.4	4
CPTU2	18.1	16.6	4
CPTU1	12.2	9.0	3
SCPTU3	15.9	15.6	4
CPTU3	15.1	13.5	4
CPTU4	11.2	8.2	3
SCPTU2	25.7	27.6	4

Table 2. Stratigraphy and geotechnical parameters of soil profile C1. The liquefiable layers are referred as LS.

layer	soil type	depth	density	S-wave velocity	P-wave velocity	earth press. coeff.	reference strain	soil sample
		m	kg/m^3	m/s	m/s		‰	
1	sandy silt (LS1)	9.7	1750	185	1234	0.96	0.39	S11-C1
2	silty clay	12.0	1800	180	465	0.7	0.48	
3	sandy silt (LS2)	14.0	1850	180	402	0.6	0.39	S11-C3
4	silty clay	21.5	1800	200	632	0.8	0.48	
5	sandy gravel	27.5	1850	275	710	0.7	0.39	S11-C3
6	silty clay	33.0	1900	280	723	0.7	0.49	
7	sandy gravel	73.0	1975	385	994	0.7	100	
8	silty clay	113	2125	595	1536	0.7	100	
	bedrock	> 113	2200	700	1807	0.7		

827 **Table 3.** Stratigraphy and geotechnical parameters of soil profile C2**.** The liquefiable layers are

828 referred as LS.

layer	soil type	depth	density	S-wave velocity	P-wave velocity	earth press. coeff.	reference strain	soil sample
		m	kg/m^3	m/s	m/s		‰	
1	sandy silt (LS1)	3.3	1700	200	894	0.9	0.39	S11-C1
2	silty clay	8.5	1750	190	601	0.8	0.48	
3	sandy silt (LS2)	12.5	1850	200	516	0.7	0.39	S11-C3
4	silty clay	20.5	1850	210	939	0.9	0.48	
5	sandy gravel	26.0	1850	275	710	0.7	0.39	S11-C3
6	silty clay	33.0	1900	280	723	0.7	0.49	
7	sandy gravel	73.0	1975	385	994	0.7	100	
8	silty clay	113	2125	595	1536	0.7	100	
	bedrock	> 113	2200	700	1807	0.7		

829

830 **Table 4.** Stratigraphy and geotechnical parameters of soil profile C3. The liquefiable layers are

831 referred as LS.

layer	Soil Type	depth	density	S-wave velocity	P-wave velocity	earth press. coeff.	reference strain	soil sample
		m	kg/m^3	m/s	m/s		‰	
1	sandy silt (LS1+LS2)	12	1800	200	516	0.7	0.39	S11-C3
2	silty clay	21.5	1850	190	491	0.7	0.48	
3	sandy gravel	25.0	1900	240	759	0.8	0.39	S11-C3
4	silty clay	31.5	1900	280	723	0.7	0.49	
5	sandy gravel	71.5	1975	385	994	0.7	100	
6	silty clay	111.5	2125	595	1536	0.7	100	
	Bedrock	> 111.5	2200	700	1807	0.7		

832

833 **Table 5.** Normalized shear modulus reduction curves G/G_0 obtained using RC tests.

Soil sample	S2-C2		S3-C3		S10-C3	
Soil type	sandy silt/gravel		silty clay		deep silty clay	
Shear ref. strain	$\gamma_{r0} = 0.39‰$		$\gamma_{r0} = 0.48‰$		$\gamma_{r0} = 0.49‰$	
	shear strain %	G/G_0	shear strain %	G/G_0	shear strain %	G/G_0
	0.00015	1.000	0.00010	1.000	0.000042	1.000
	0.00030	1.000	0.00020	1.000	0.000075	1.000
	0.00064	1.000	0.00033	1.000	0.000165	1.000
	0.00097	0.995	0.00061	0.996	0.000315	1.000
	0.00161	0.982	0.00106	0.985	0.000550	1.001
	0.00245	0.966	0.00175	0.961	0.000784	1.001
	0.00406	0.926	0.00328	0.925	0.001209	1.001
	0.00583	0.890	0.00583	0.868	0.001561	1.001
	0.01159	0.810	0.00905	0.819	0.002307	1.002
	0.02178	0.692	0.01688	0.719	0.003178	0.996
	0.04659	0.509	0.03310	0.529	0.004950	0.968
	0.07419	0.400	0.07133	0.331	0.006578	0.947
	0.20062	0.197			0.008409	0.928
					0.014088	0.838
					0.022048	0.719
					0.038053	0.550
					0.074181	0.390
					0.199728	0.208
					0.289764	0.163

834

835

836 **Table 6.** Liquefaction parameters used to calibrate CTX test curves

			Soil sample			
			S11-C1-1	S11-C1-2	S11-C3-2	S11-C3-3
Density	ρ	kg/m^3	1950	1950	2050	2050
S-wave velocity	v_s	m/s	175	175	152	152
P-wave velocity	v_p	m/s	2480	2480	2149	2149
Reference strain	γ_r	‰	0.11	0.11	0.15	0.15
Friction angle	α	°	29	29	32	32
Dilatation angle	ϕ_p'	°	25	25	26	26
Cell pressure	p_0	kN/m^2	300	300	300	300
Back pressure	u_0	kN/m^2	200	200	200	200
	c_1		5.0	4.9	5.2	5.0
	S_1		0.005	0.005	0.005	0.005
	p_1		0.4	0.4	0.4	0.4
	p_2		0.6	0.6	0.6	0.6
	w_1		5.9	6.2	6.5	6.0

837

838 **Table 7.** Peak ground acceleration in *x*- and *y*-direction for the different water table depth z_w

Soil profile											
C1				C2				C3			
	z_w	a_x	a_y		z_w	a_x	a_y		z_w	a_x	a_y
	m	m/s^2	m/s^2		m	m/s^2	m/s^2		m	m/s^2	m/s^2
TSA		1.40	1.37	TSA		1.46	1.60	TSA		1.55	1.61
ESA	6.8	1.68	1.61	ESA	6.2	2.23	1.81	ESA	3.7	2.10	1.87
ESA	5.8	1.68	1.59	ESA	5.2	2.23	1.81	ESA	2.7	**3.21**	2.27
ESA	4.8	1.72	1.63	ESA	4.2	2.22	1.72	ESA	1.7	**4.02**	2.22

839

840

841 **FIGURE CAPTIONS**

842 (a) (b)

843

844

845

846

847

848 (c) (d)

849

850

851

852

853

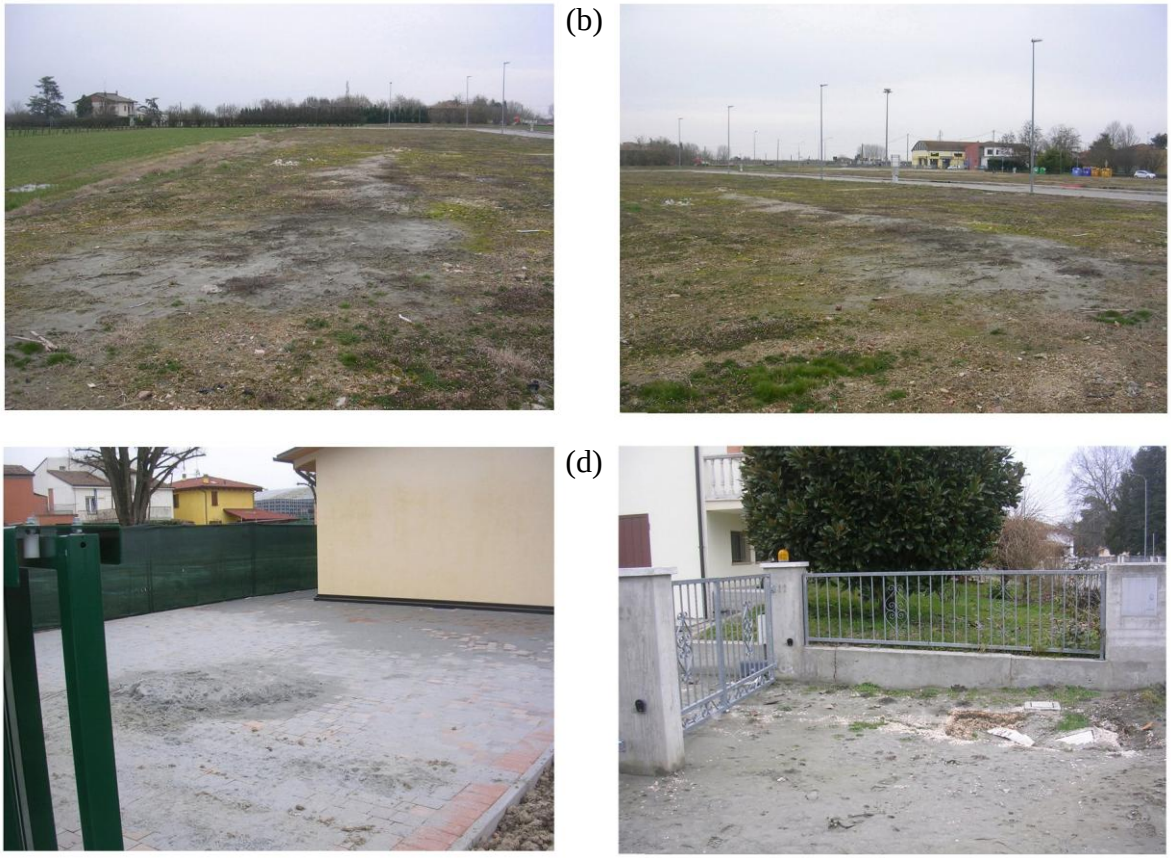

854 **Figure 1.** Liquefaction effects observed at San Carlo village after the 20 May 2012 M_w 5.9
855 earthquake: a, b) evidences of clay spread out on free field; c, d) evidence of clays spread out
856 from building foundations causing damage to structures.

857

858

859

860

861

862

863

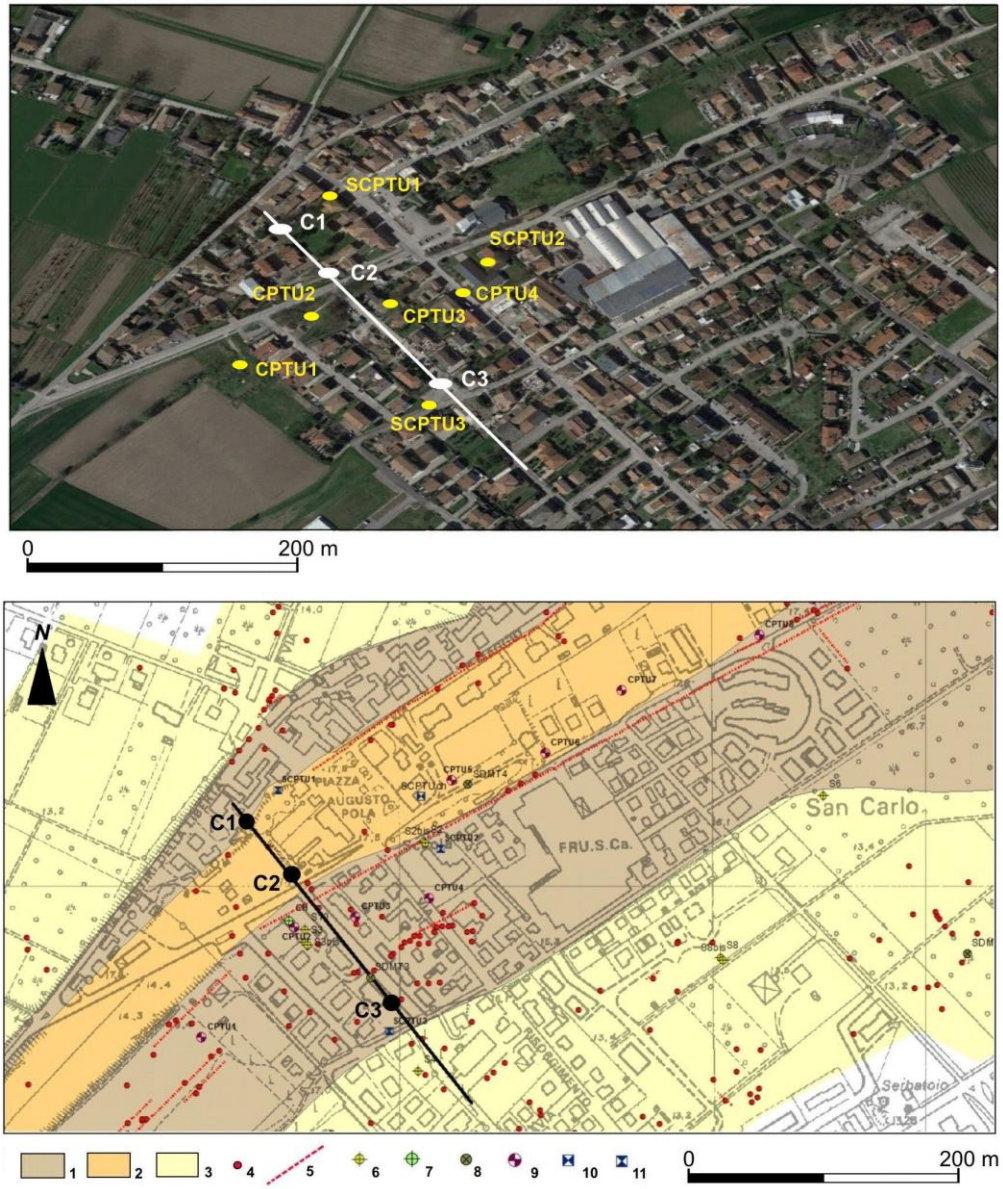

Figure 2. (a) Google Earth satellite view of the San Carlo village with trace of geological cross section and location of modelled soil columns. (b) geological map of the San Carlo village: 1) deposits of river channel; 2) deposits of river banks; 3) deposits of alluvial plain; 4) liquefaction

sand boil; 5) liquefaction trench; 6) borehole with samples; 7) borehole without samples; 8) Seismic DilatoMeter Test (SDMT); 9) Cone Penetration Test with piezocone (CPTU); 10) Seismic Cone Penetrometric Test with piezocone (SCPTU); 11) Seismic Cone Penetrometric Test (SCPT). (c) Geological cross section: 1) Holocene liquefiable deposits; 2) Holocene not liquefiable deposits; 3) Pleistocene liquefiable deposits; 4) Pleistocene non liquefiable deposits; 5) not classified Pleistocene deposits; 6) water table; 7) liquefaction sand boil; 8) liquefaction trench; 9) borehole; 10) CPTU or SCPT test; 11) modelled soil columns.

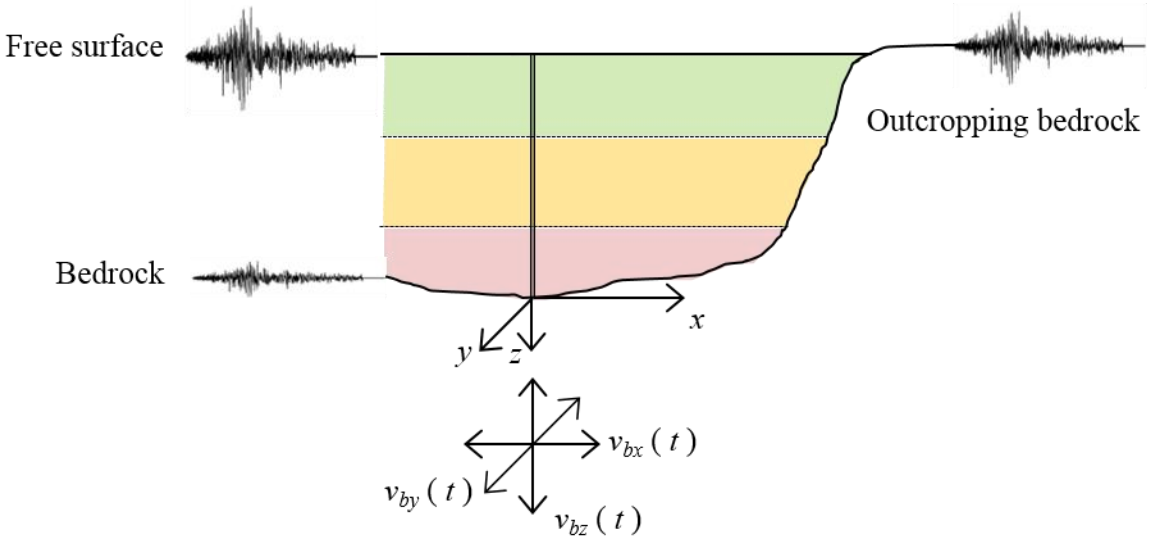

Figure 3. Spatial discretization of a horizontally layered soil. The seismic loading applied at the bedrock level is a deconvolved outcropping signal in terms of velocity.

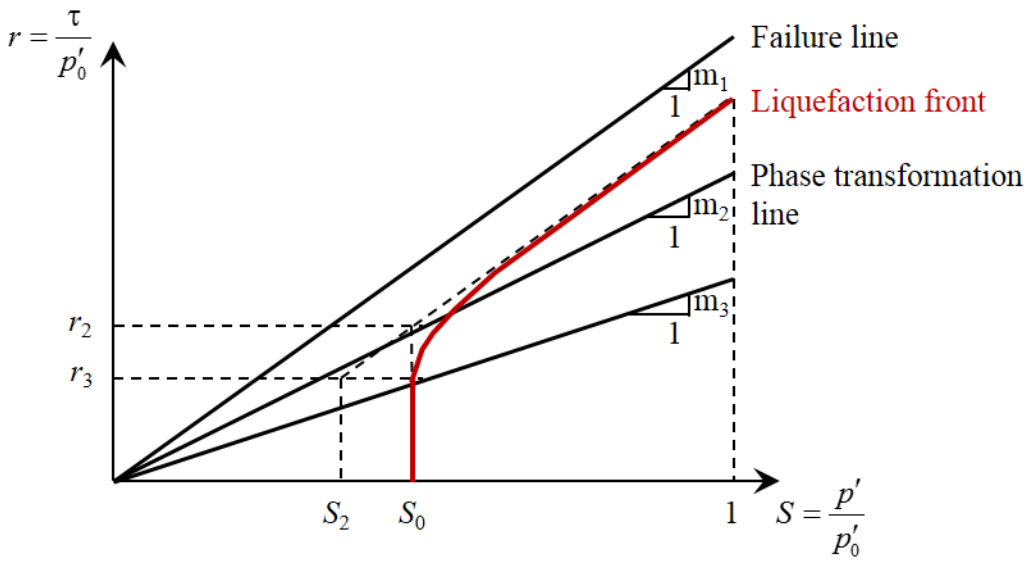

898

899 **Figure 4.** Liquefaction front $r(S)$, where r is the deviatoric stress ratio and S is the state

900 variable.

901

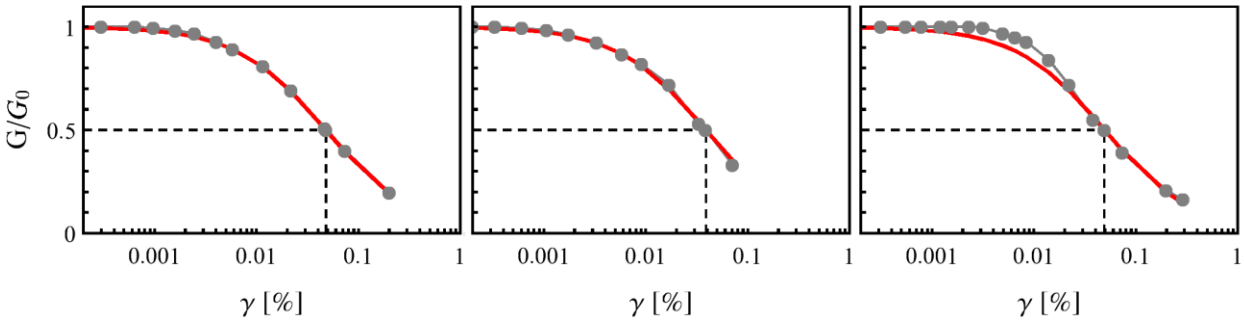

902

903 **Figure 5.** Normalized shear modulus reduction curves obtained using RC test results (markers)

904 and fitted using the hyperbolic model (solid line), for soil samples S2-C2 (left) having reference

905 shear strain $\gamma_{r0} = 0.48‰$, S3-C3 (middle) having $\gamma_{r0} = 0.39‰$ and S10-C3 (right) having

906 $\gamma_{r0} = 0.49‰$.

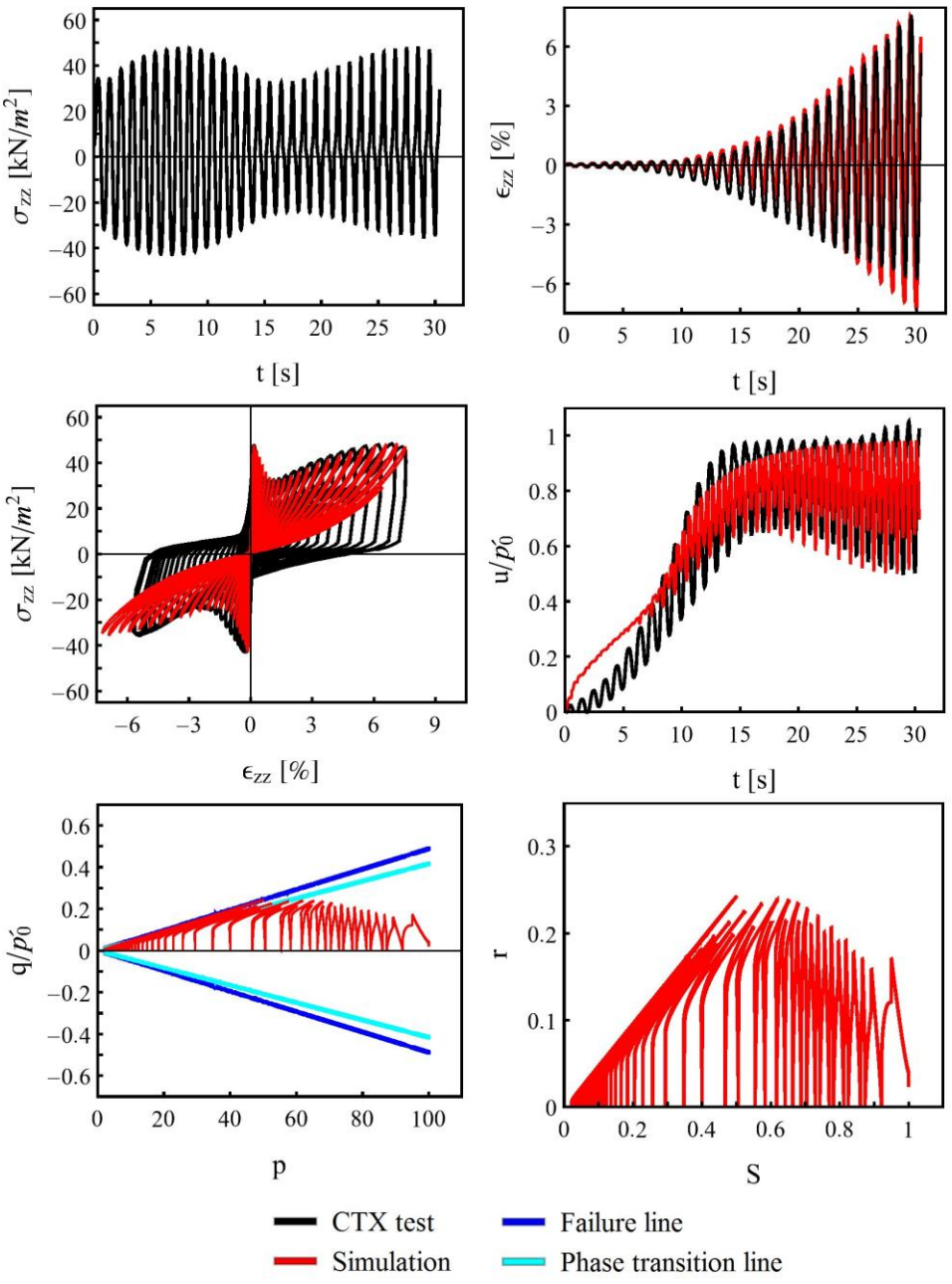

907

908 **Figure 6.** Fitting of cyclic Consolidated Undrained triaxial test curves to calibrate liquefaction

909 parameters, for S11-C1-2 soil sample in LS1 liquefiable soil layer.

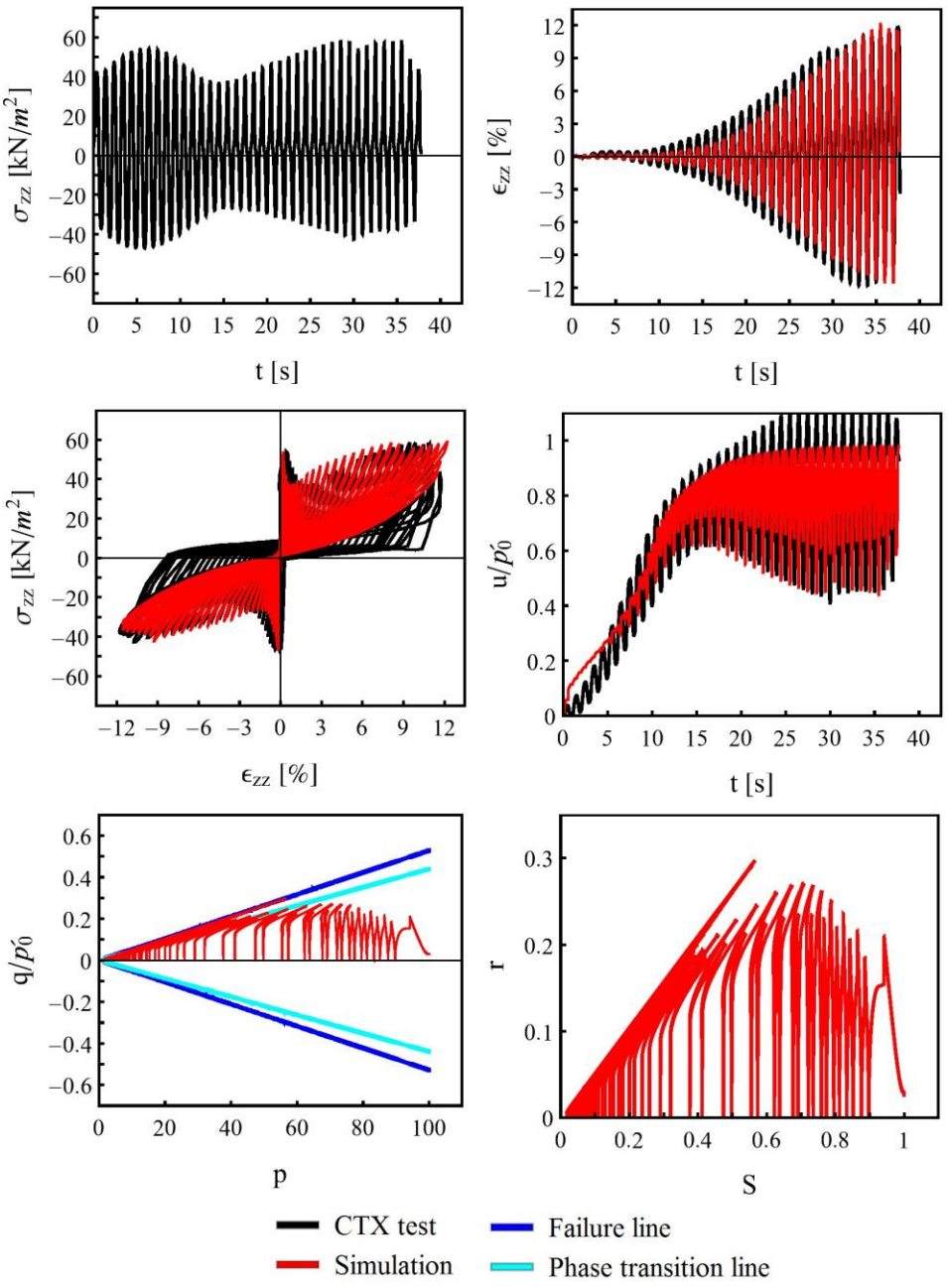

910

911 **Figure 7.** Fitting of cyclic Consolidated Undrained triaxial test curves to calibrate liquefaction

912 parameters, for S11-C3-3 soil sample in LS2 liquefiable soil layer.

913

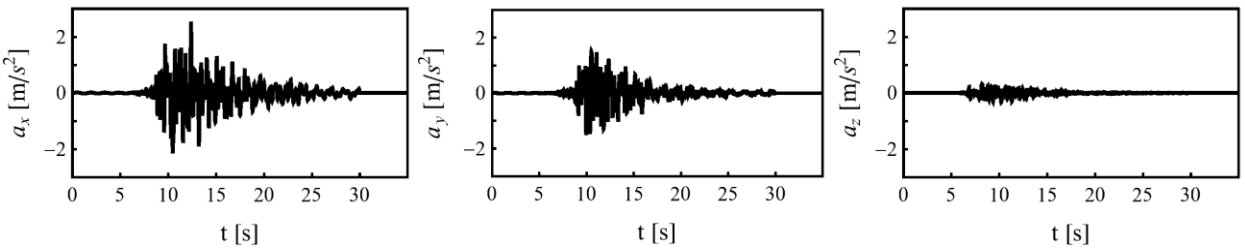

914

915 **Figure 8.** Three components of the incident motion applied at the soil-bedrock interface in terms

916 of acceleration. The peak acceleration is 2.54 $\mathrm{m/s^2}$ in x -direction, 1.51 $\mathrm{m/s^2}$ in y-direction and

917 0.33 $\mathrm{m/s^2}$ in z-direction.

918

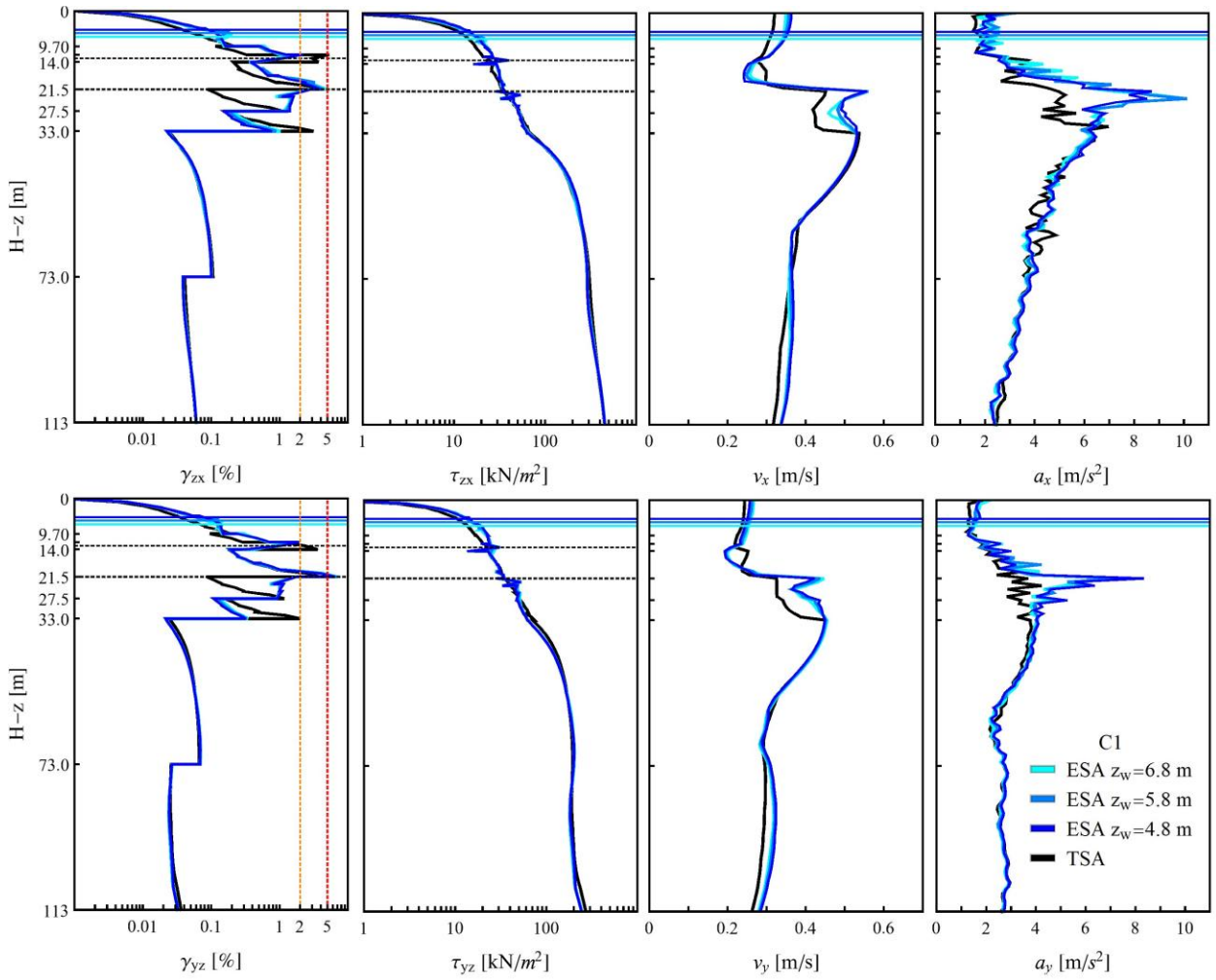

Figure 9. Profiles with depth of maximum shear strain and stress, horizontal velocity and acceleration, during the seismic event, for different water table depth and for TSA conditions in the C1 soil column. The horizontal dashed lines indicate the depth where the shear stress-strain loops are analyzed.

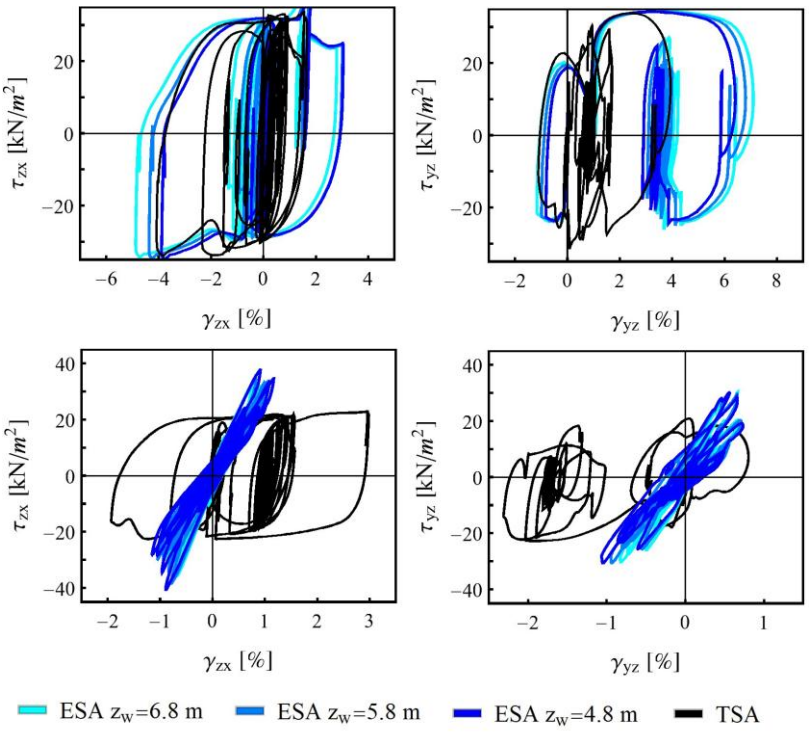

924

925 **Figure 10.** Hysteresis loops in C1 soil profile for different water table depth and for TSA
926 conditions: (top) at 21.5 m in a non liquefiable soil layer; (bottom) at 13 m in LS2 liquefiable
927 soil layer.

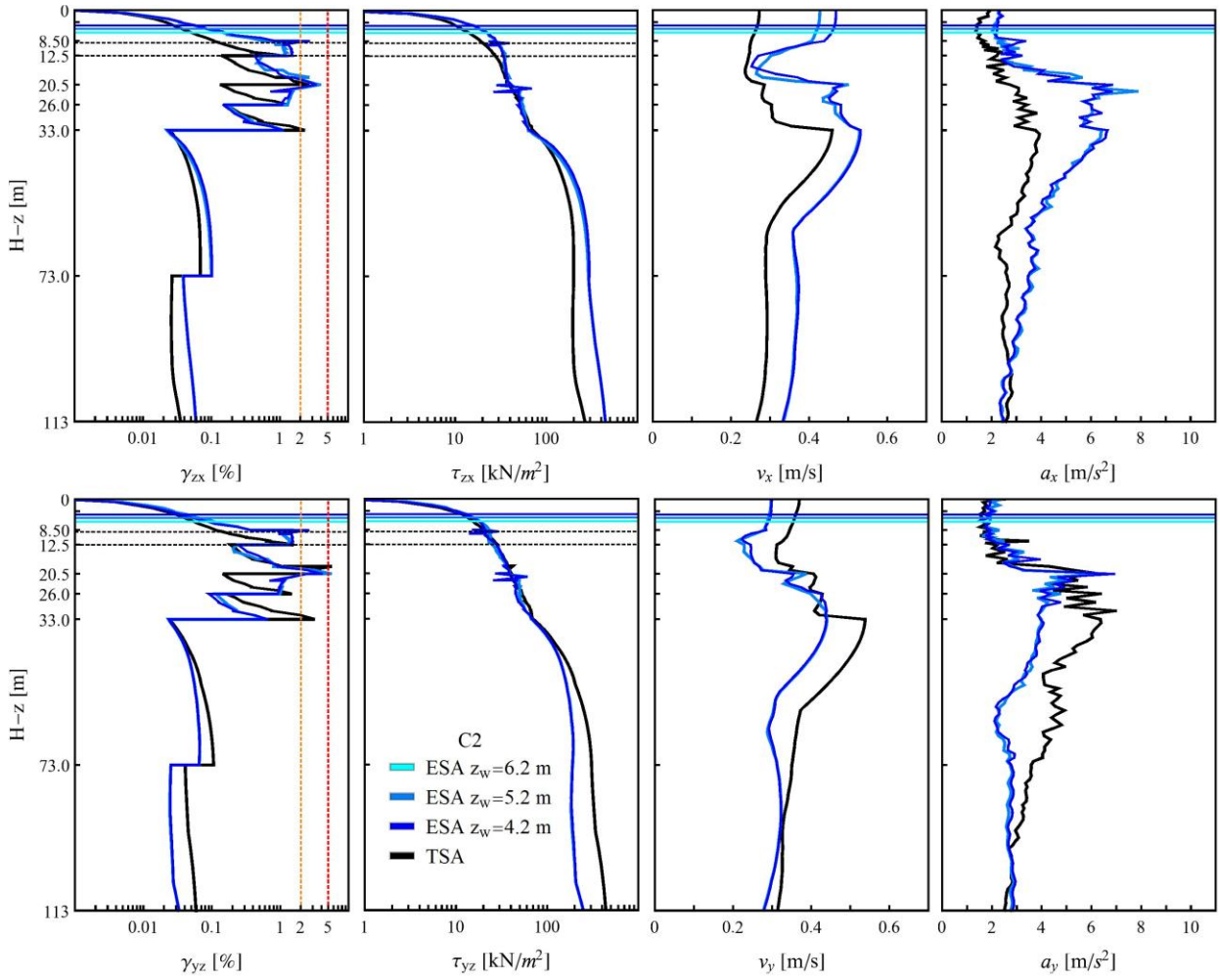

928

929 **Figure 11.** Profiles with depth of maximum shear strain and stress, horizontal velocity and
930 acceleration, during the seismic event, for different water table depth and for TSA conditions in
931 the C2 soil column. The horizontal dashed lines indicate the depth where the shear stress-strain
932 loops are analyzed.

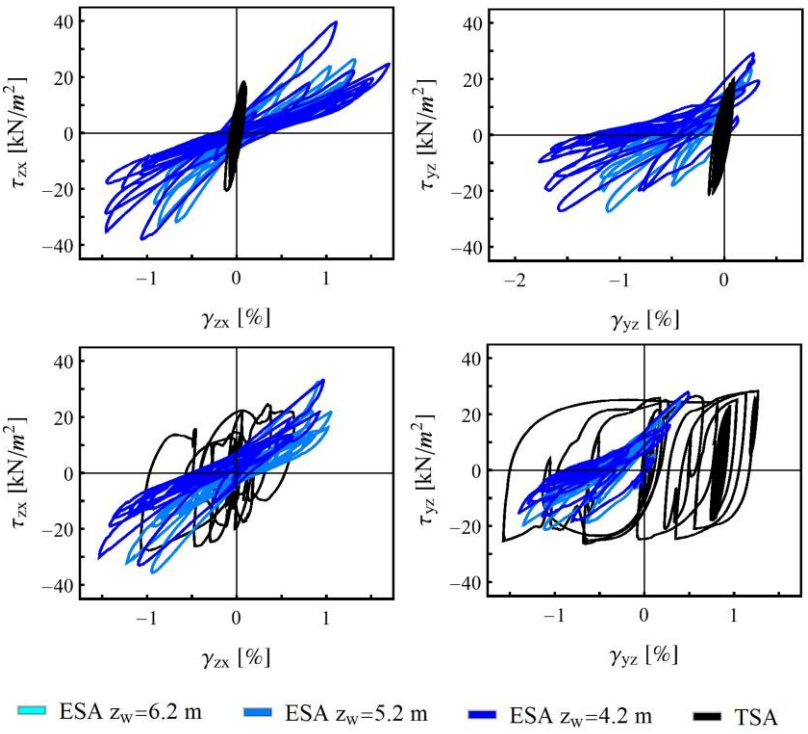

933

934 **Figure 12.** Hysteresis loops in C2 soil profile for different water table depth and for TSA

935 conditions: at 9 m (top) and at 12.5 m (bottom) in LS2 liquefiable soil layer.

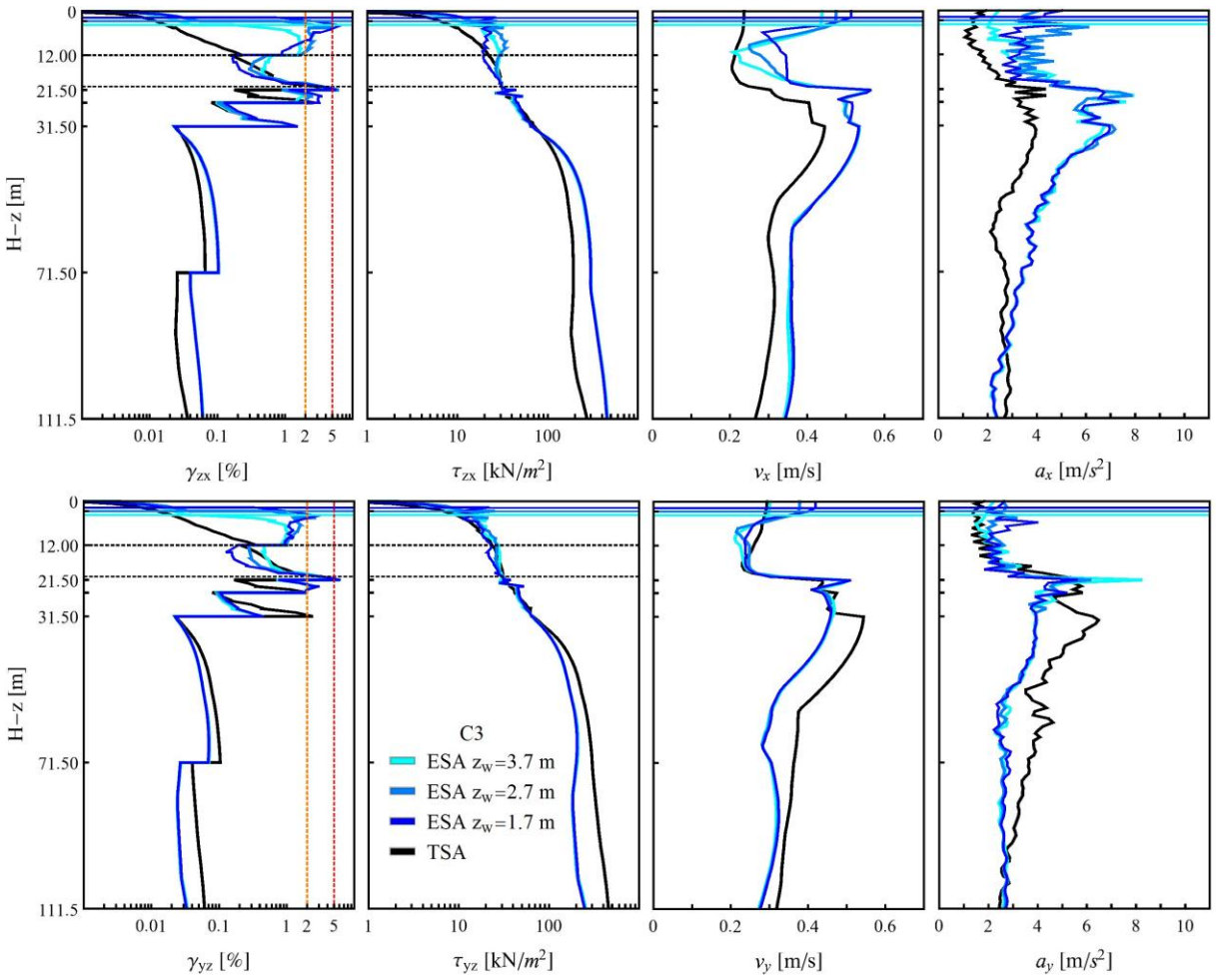

936

937 **Figure 13.** Profiles with depth of maximum shear strain and stress, horizontal velocity and
938 acceleration, during the seismic event, for different water table depth and for TSA conditions in
939 the C3 soil column. The horizontal dashed lines indicate the depth where the shear stress-strain
940 loops are analyzed.

941

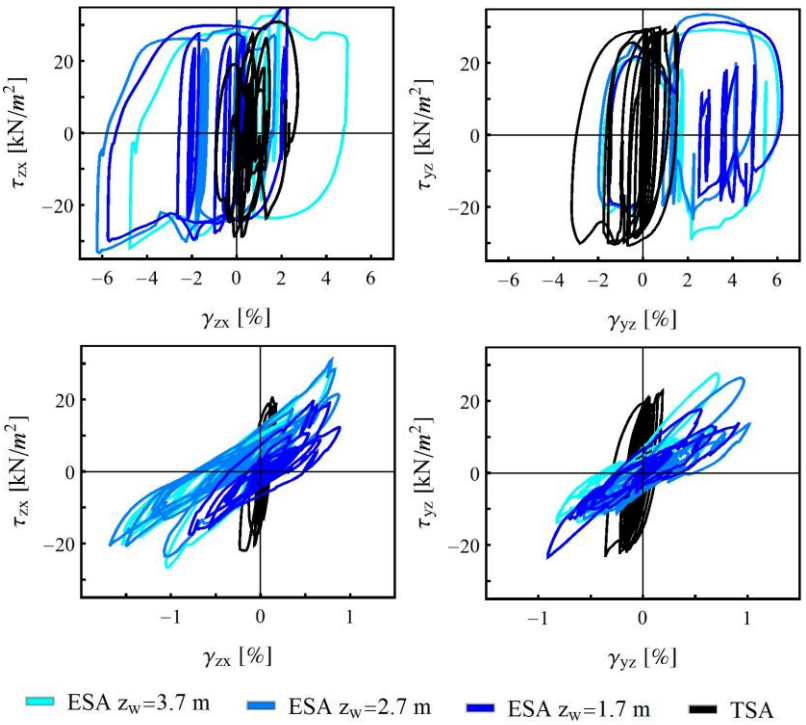

942

943 **Figure 14.** Hysteresis loops in C3 soil profile for different water table depth and for TSA
944 conditions: (top) at 20.5 m in a non liquefiable soil layer; (bottom) at 12 m in LS1+LS2
945 liquefiable soil layer.

946

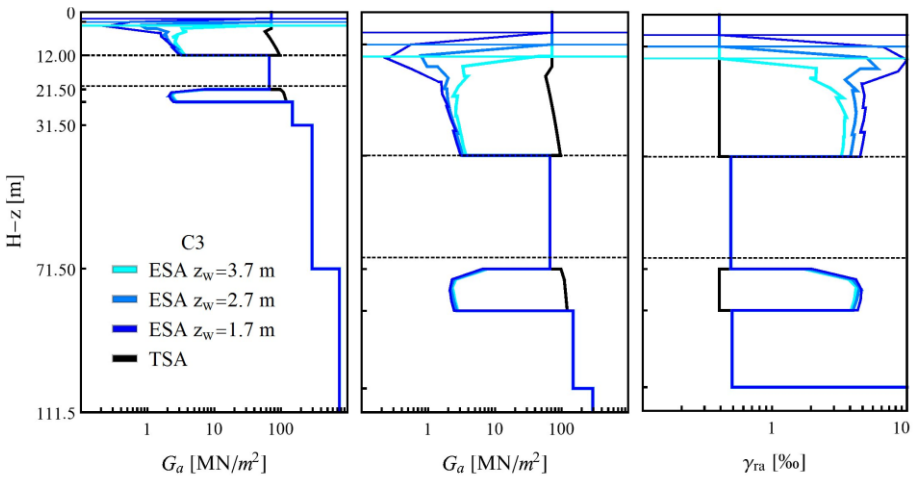

947

948 **Figure 15.** Profile with depth of minimum shear modulus (left), during the seismic event, with
949 zoom in the first soil layers (middle) and profile with depth of the maximum reference shear
950 strain, for different water table depth and for TSA conditions, in the C3 soil profile. The
951 horizontal dashed lines indicate the depth where the shear stress-strain loops are analyzed.

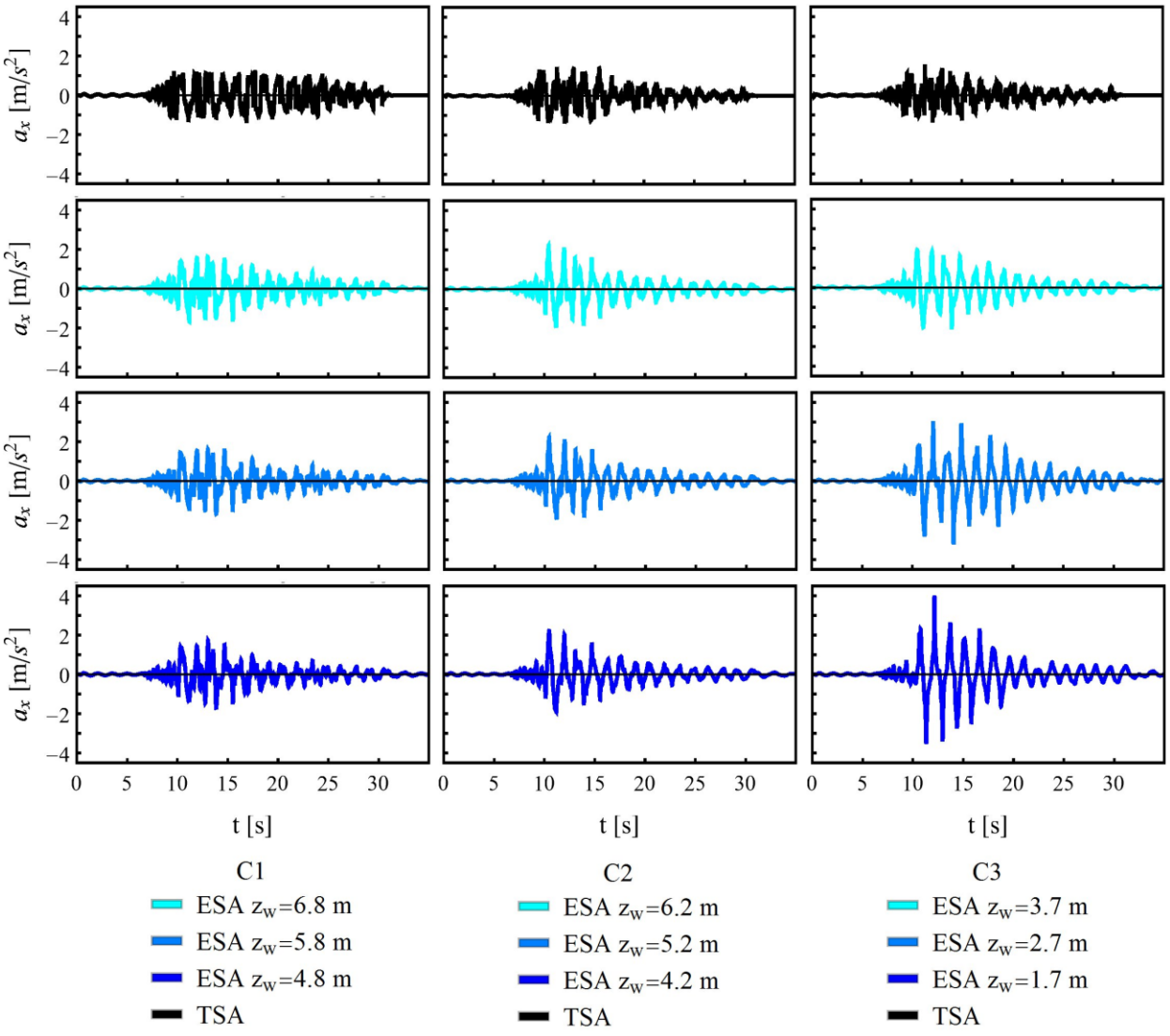

952

953 **Figure 16.** Acceleration time history at the ground surface for C1 (left), C2 (middle) and C3

954 (right) soil profiles, in *x*-direction, for different water table depth and for TSA conditions.

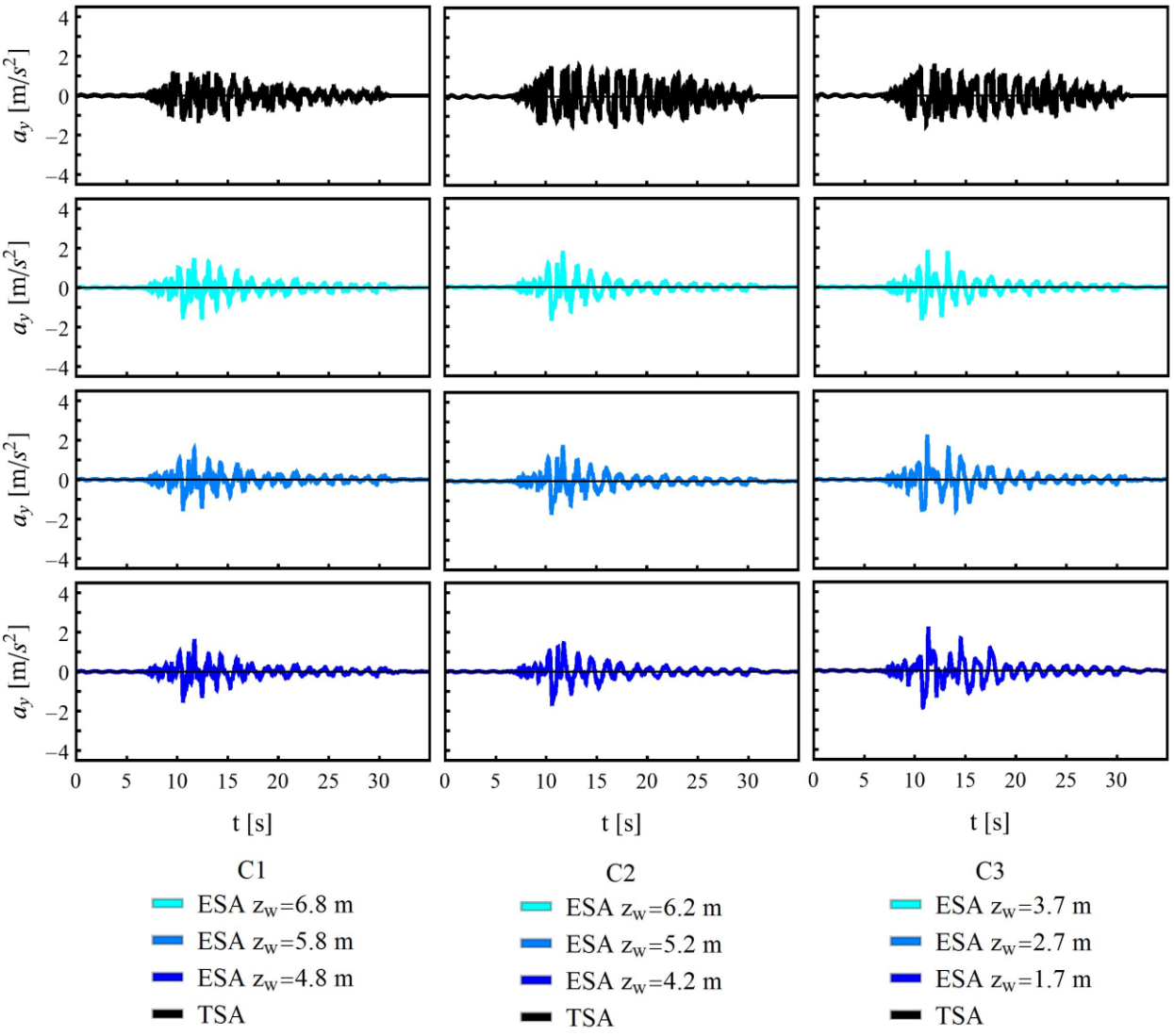

955

956 **Figure 17.** Acceleration time history at the ground surface for C1 (left), C2 (middle) and C3

957 (right) soil profiles, in *y*-direction, for different water table depth and for TSA conditions.

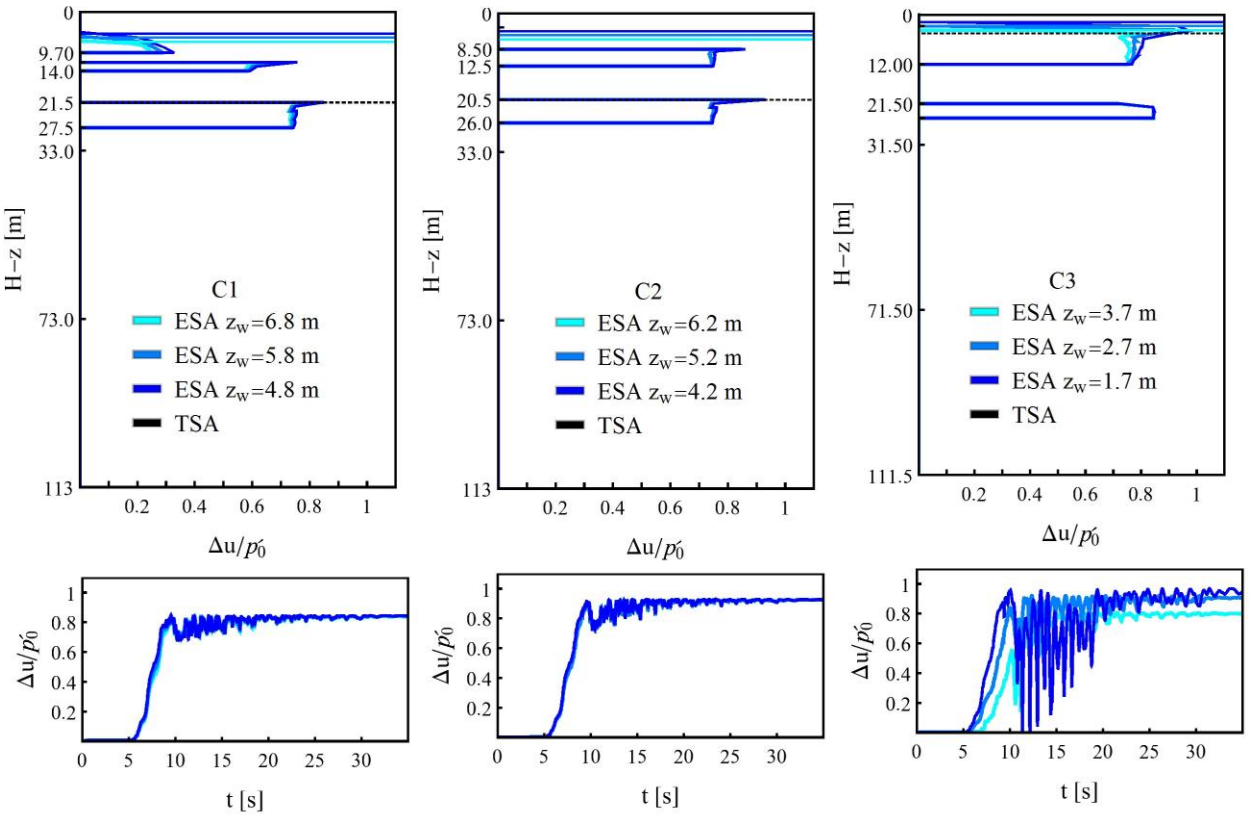

958

959 **Figure 18.** Excess pore water pressure, normalized with respect to the average effective pressure,
960 for different water table depth, in C1 (left), C2 (middle) and C3 (right) soil columns: (top)
961 Profiles with depth of maximum value during the seismic event. The horizontal dashed lines
962 indicate the depth where the time histories are analyzed. (bottom) Time history: at 21.5 m (LS1)
963 in C1 soil profile, at 20.5 m (LS2) in C2 soil profile and at 4.5 m (LS1+LS2) in C3 soil profile,
964 for $z_w = 3.7\,\mathrm{m}$, at 3.5 m for $z_w = 2.7\,\mathrm{m}$ and $z_w = 1.7\,\mathrm{m}$.